Coastal Engineering 131 (2018) 88–105

Contents lists available at ScienceDirect

Coastal Engineering

journal homepage: www.elsevier.com/locate/coastaleng

A partial cell technique for modeling the morphological change and scour

Zhong Peng [a], Qing-Ping Zou [b,c,*], Pengzhi Lin [c]

[a] Metocean Modelling and Analysis, Fugro GB Marine Ltd., Wallingford, OX10 9RB, UK
[b] The Lyell Centre for Earth and Marine Science and Technology, Institute for Infrastructure and Environment, Heriot-Watt University, Edinburgh, UK
[c] State Key Laboratory of Hydraulics and Mountain River Engineering, Sichuan University, 610065, Chengdu, China

ARTICLE INFO

Keywords:
Morphological model
Seawall
Toe scour
Standing wave
Breaking wave
RANS
VOF
Partial cell
Cut cell

ABSTRACT

A novel partial cell technique applied on structured grids is developed to track the deformation of water-soil interface associated with beach morphological change and toe scour in front of coastal structures. It allows the use of the same orthogonal structured grids for morphological, sediment transport and hydrodynamic models therefore, has the advantage of consuming less CPU and without the need to adapt grids to the evolving beach morphology. An improved sand-slide model with better mass conservation is introduced to resolve the avalanche behaviour of the sediment motion. The RANS-VOF hydrodynamic model has been extended to cope with complex bathymetry. The newly developed numerical model suite, coupling the RANS-VOF model, a bedload sediment transport model and a morphological model using the partial cell technique, are validated against the analytical solutions and laboratory measurements for different incoming wave conditions, local water depths and bottom slopes. This study reveals the key processes that govern the behaviour of beach morphology change in front of a vertical coastal structure during storms. The model-data comparisons demonstrate the robustness of partial cell technique to capture the movement of the water-soil interface.

1. Introduction

Coastal flooding occurs when a flood defence fails. This happens when the storm conditions surpass what the defence was designed for (functional failure) or the defence is damaged and therefore does not function as expected (structural failure). Structural failures are unexpected, therefore, more dangerous and have been the cause of recent major flooding events (CIRIA 1986; Zou et al., 2013). During severe storms, excessive overflow or wave overtopping and toe scour at the costal defence are the two leading causes of structural failure. The former occurs in the presence of high water level due to surge and wave set-up, therefore low freeboard (vertical distance from the crest of the defence to the water level) and large waves and may erode the leeward face and crest of the defence and damage the armour layers. The latter is the erosion of the foreshore at the base of the defence that may undermine the structure (e.g. CIRIA 1986). This study will focus on the beach morphological changes and toe scour processes that lead to failure of defences and flooding.

Beach slope and profile in front of the defence are an important design consideration of sea defences. Bed level at the defence may be reduced by several meters in a large storm. This beach lowing would increase the still water depth at the structure; therefore, allow larger waves to arrive at the structure without breaking. In turn larger waves lead to more beach lowering and wave overtopping and larger wave loading and the process continues and form a positive feedback that eventually undermines the structure (Zou and Reeve, 2009).

Steady streaming and wave breaking are significant controlling factors in sediment transport and beach profile changes around a coastal structure. The experimental study by Fredsøe and Sumer (1997) demonstrates that the steady streaming and plunging breaker generates a scour hole in front of and at the lee-side of the breakwater respectively. Tsai et al. (2009) conducted laboratory experiments of toe scour in front of a Seawall on a beach slope of 1:5 under regular waves. They found that the scour depth produced by a plunging breaker is larger than that by a spilling breaker or a non-breaking wave. Young and Testik (2009) carried out a laboratory study of two-dimensional onshore scour along the base of submerged vertical and semi-circular breakwaters on both sloping and horizontal sandy bottoms and found that the characteristics of scour are independent of breakwater shape or type.

In case of non-breaking waves, Sumer and Fredsøe (2000) and Sumer (2007) found that the reflection from the breakwater forms a standing wave which generates the steady streaming in front of the breakwater, consisting of top and bottom recirculating cells. The formation of bottom cell is related to the boundary layer over the bed and the near bed

* Corresponding author. The Lyell Centre for Earth and Marine Science and Technology, Institute for Infrastructure and Environment, Heriot-Watt University, Edinburgh, UK.
E-mail addresses: z.peng@fugro.com (Z. Peng), qingping.zou@gmail.com (Q.-P. Zou), cvelinpz@126.com (P. Lin).

https://doi.org/10.1016/j.coastaleng.2017.09.006
Received 8 August 2016; Received in revised form 9 August 2017; Accepted 9 September 2017
Available online 10 November 2017

sediment motion responds to these recirculating cells. Consequently a scour and deposition pattern in front of the breakwater emerges in the form of alternating scour and deposition areas lying parallel to the structure. However, in case of breaking waves, the complex process of wave breaking generates a strong downward jet to erode the bed and mobilize the sediment at the toe of a vertical wall, which presumably leads to scour at the toe of a seawall (Sumer, 2007).

Earlier numerical models for predicting scour at sea walls include those by Rakha and Kamphuis (1997) which is built upon a phase resolving Boussinesq wave model. Although this type of studies represent progress, they do not adequately address the complex physics arising from the wave breaking, streaming and turbulence near the bed and coastal structure as discussed above. As with the majority of beach morphological models, these models are depth averaged and unable to resolve the eddies in the immediate proximity of the sea wall; and therefore fail to predict toe scour (Rakha and Kamphuis, 1997). Lin and Liu (2003) concluded that the RANS (Reynolds Averaged Navier-Stokes Solver) models by Lin and Liu (1998) can run for a long time until the wave reaches a quasi-steady state, providing an accurate flow field for the simulation of sediment transport in the surf zone. Recently this model has been further developed and used widely to investigate wave-structure interactions and subsequent coastal flood risks (Garcia et al., 2004; Lara et al., 2006; Losada et al. (2008); Peng and Zou 2011; Zou and Peng 2011; Zou et al., 2012).

Gislason et al. (2009a) applied a Navier-Stokes solver to examine the energy and momentum flux and the streaming velocity for standing waves in front of a fully reflecting wall. Hajivalie and Yeganeh-Bakhtiary (2009) used a numerical model based on Reynolds Averaged Navier-Stokes (RANS) equations and a k-ε turbulence model to study the effect of breakwater steepness on the hydrodynamic characteristics of standing waves. Later on, Yeganeh-Bakhtiary et al. (2010) found that the recirculating cells of steady streaming were generated in front of vertical breakwaters in the presence of fully standing waves but not partially standing waves.

Following Pedrozo-Acuña et al., 2006; Yeganeh-Bakhtiary et al., 2010, Gislason et al. (2009b), the bed profile is updated by solving the sediment conservation equation based on the time-averaged sediment transport rates predicted by the bed-load sediment transport equation by Fredsøe and Deigaard (1992) using the hydrodynamics predictions by the phase-resolved RANS-VOF model. Due to the complexity of sediment transport process, the instantaneous sediment transport rate is normally calculated by empirical formulae derived from experiments, e.g. Meyer-Peter and Mueller (1948) and Madsen (1991). We adopt this approach since it is able to capture the bed profile change and is more robust than the fluid and soil two-phase model by Hajivalie et al. (2012).

Many state-of-art morphological models use the classical lower order Lax–Wendroff or modified Lax–Wendroff schemes and becomes unstable after a long simulation time. Therefore, Long et al. (2008) investigated the stability and performance of several finite difference schemes and recommended a fifth order Euler-WENO scheme for wave phase-resolving sediment transport models. In order to resolve the slumping of sandy materials, Liang and Cheng (2005) proposed a sand-slide model to account for the avalanche without consideration of the mass conservation of bed materials. More recently, Jacobsen (2015) proposed a geometric sand sliding routine on unstructured grids to assure the mass conservation in computational morphodynamics. In this study, we will extend Liang and Cheng (2005) sand sliding model by improving its mass conservation since the present hydrodynamics model and their model are both based on a structured grid.

Liang and Cheng (2005) used a RANS model to successfully simulate the observed wave induced scour behaviour beneath a submarine pipeline. Marieu et al. (2008) developed a morphology module in combination with an existing RANS model to study vortex ripple morphodynamics. Liu and García (2008) applied a RANS-VOF model to simulate the local scour at the bridge piers. Khosronejad et al. (2012) coupled a RANS model with a morphological model and immersed boundary method to study the scour around bridge piers of three different shapes. Baykal et al. (2015) used a 3D RANS model coupled with a morphological model to examine the flow and scour patterns around a vertical cylinder in a steady current. Only recently has the RANS-VOF (Volume-Of-Fluid) numerical modelling been used to study the scour process at coastal structures. Gislason et al. (2009b) investigated the two-dimensional scour and deposition in front of vertical and sloping Seawalls by coupling a 3-D Navier-Stokes solver with a k-ω turbulence model and a morphological model. They were able to reproduce the well-known alternating scour and deposition pattern in front of the breakwater (e.g., Sumer and Fredsøe, 2000). The free surface was tracked by integrating in time the kinematic boundary conditions based on the free surface volume flux, therefore, wave breaking is not resolved in their study. Tofany et al. (2014, 2016) applied the RANS-VOF model to simulate scour and overtopping in front of a vertical breakwater for different wave conditions. Their work was limited to standing or partial standing waves over a flat bottom in front of the structure. Wave breaking was not considered either. On the other hand, Hajivalie et al. (2012) applied an Euler–Lagrange flow and soil two-phase model to examine the scour in front of a vertical breakwater. The sediment phase was treated as an assembly of discrete sand grains and the scour was predicted as the motion of a granular media using a Lagrangian approach.

More recently, Jacobsen et al. (2014a, 2014b) successfully simulated the formation and development of a breaker bar under regular waves using the OpenFOAM (Open Field Operation and Manipulation) which is an open source code of two phase RANS-VOF flow model (Jasak, 1996; Weller et al., 1998; Jacobsen et al., 2012), by considering both bedload and suspended sediment transport. Besides the hydrodynamic model grid, they adopted a separate set of mesh for bedload transport and morphology model and another set of mesh for suspended sediment transport model, which is similar to the hydrodynamic mesh but without the near bottom cells. Their model results at these three sets of grids are synchronized frequently and validated against the laboratory study by Scott et al. (2005) for breaking waves over a fixed bar and the experiment by Baldock et al. (2011).

In this study, a novel partial cell technique on structured grids is developed to track the location of the evolving water-soil interface. This method is in analogy with the VOF method. It has a number of advantages over the traditional method used in morphological modelling. For example, it enables us to use the same orthogonal structured grids for morphological, sediment transport and hydrodynamic models and avoid adapting grids to the evolving beach morphology, therefore, consume less CPU and minimize the potential discontinuity issues at the water–soil interface and the resulting model instability. An improved sand-slide model with better mass conservation of bed materials is introduced to resolve the avalanche behaviour of the sediment motion. The RANS-VOF hydrodynamic model is combined with a bedload sediment transport model and a morphological model to predict the beach profile changes and toe scour on both flat bottom and a sloping sandy beach in front of a vertical Seawall. In order to get a better handle on the initial beach profiles in the simulations, the RANS-VOF model has been further extended to cope with complex bathymetry, such as a ripple bed.

2. Model description

A hydrodynamic model and a bed-load sediment transport model have been combined with a morphological model to investigate the hydrodynamics of wave interactions with a seawall behind a sandy beach slope and the control factors of beach profile change and toe scour in front of vertical seawalls (Zou et al., 2012).

2.1. Hydrodynamic model

The Reynolds Averaged Navier-Stokes solver with a Volume-of-Fluid free surface capturing scheme (RANS-VOF) by Lin and Liu (1998) has been further developed in the past years and will be further extended

here as the hydrodynamic model. In this model, the non-linear k–ε equations are employed to obtain the turbulent kinetic energy, k, its dissipation rate, ε, the eddy viscosity and then the Reynolds stress (Lin and Liu, 1998). We decided to use this turbulence model as it can provide the overall good simulation results for the wave structure interaction and the wave-induced bottom boundary layer can be reasonably captured. The governing equations and boundary conditions for the turbulence model are provided in the Appendix. The present RANS-VOF model employs the finite difference method on staggered grids to solve the momentum equations to obtain the velocities, pressure gradients and turbulence parameters. During the computation, a free slip boundary condition at the solid boundaries and a zero-stress condition at the free surface are employed. An active wave generating and absorbing wave-maker is applied at the inlet to generate waves and simultaneously absorb the reflected waves from the structures (Troch and De Rouck, 1999). This type of RANS-VOF approach has been used extensively to study surf zone and swash zone problems (Lubin et al., 2006; Zhao et al., 2004; Christensen, 2006; Wang et al., 2009; Pedrozo-Acuna et al., 2010; Bakhtyar et al., 2010; Xie, 2012). More detailed information about the hydrodynamic model used here can be found in Lin and Liu (1998), Peng and Zou (2011), Zou and Peng (2011) and Zou et al. (2012).

In addition, in the present study, this RANS-VOF model has been further extended to cope with the complex bathymetry associated with the beach morphological changes, such as a ripple bed. In the original code, the bathymetry is defined by a series of conic sections whose equations are provided by the user. This approach is too tedious and time consuming for large and complicated bathymetry. In the updated code, complicated bathymetry can be read directly from an input file.

2.2. Sediment transport model

The bed profile is updated by solving the sediment mass conservation equation based on the time-averaged sediment transport rates from a well-established bed-load sediment transport formula (Fredsøe and Deigaard, 1992, chapter 11):

$$(1-n)\frac{\partial z_b}{\partial t} = -\frac{\partial q(x,t)}{\partial x} \tag{1}$$

where z_b is the bed level, $q(x,t)$ is the instantaneous sediment transport rate, n is the beach porosity and $n = 0.44$ is used in this study.

Previous studies (e.g., Pedrozo-Acuña et al., 2006; Bakhtyar et al., 2009) calculate the sediment transport rate using empirical formulae extracted from experimental data. Based on the work by Meyer-Peter and Mueller (1948), Madsen (1991) proposed the following formula to account for bed slope and angle of repose effects,

$$\frac{q(t)}{\sqrt{(s-1)gd_{50}^3}} = \frac{C}{1+\frac{\tan\beta}{\tan\varphi}}(\theta-\theta_c)^{3/2}\frac{u_b}{|u_b|} \tag{2}$$

where $q(t)$ is the instantaneous sediment transport rate, $s = \rho_s/\rho$ the specific density, ρ_s the grain density, ρ the water density, d_{50} the mean grain diameter, g the gravitational acceleration, C the sediment transport efficiency with a default value of 12, $\tan\beta$ the beach slope, φ the angle of repose, u_b the instantaneous free stream horizontal wave orbital velocity close to the bed, $\theta = \frac{0.5 f u_b^2}{(s-1)gd_{50}}$ the Shields parameter, θ_c is the critical Shields parameter at the threshold of motion, and f is the grain roughness bottom friction factor which is dependent on the Nikuradse grain roughness $2.5d_{50}$ relative to the water particle excursion amplitude $a = u_b/\omega$ (Smyth and Hay, 2003; Zou, 2004). The bed shear stress $\tau_b = 0.5 f u_b^2$ in Shields parameter is actually computed by the numerical model, which can be used to calculate the bedload transport. In fact, in most of cases its value is rather close to that given by the quadratic formula. However, in the vicinity of local dune or ripple, the directly computed shear stress may exhibit fluctuation. For this reason, we decide to adopt the quadratic formula which can provide smoother variation of shear stress. This formula has been widely used in the swash zone of sandy beaches (e.g., Butt and Russell, 2000; Larson et al., 2001) and sheet flow bedload transport (Gonzalez-Rodriguez and Madsen, 2007) and will be employed to calculate the sediment transport rate in this study.

A threshold shear stress for sediment motion on a bed slope of $\tan\beta$ is given by the following formula for the near bed flow in the up- and down-slope direction respectively.

$$\theta_{\beta c} = \theta_c \cos\beta\left(1-\frac{\tan\beta}{\tan\varphi}\right) \tag{3}$$

$$\theta_{\beta c} = \theta_c \cos\beta\left(1+\frac{\tan\beta}{\tan\varphi}\right) \tag{4}$$

where $\theta_{\beta c}$ and θ_c are the critical Shields parameters for the initiation of sediment motion at a sloping bed and horizontal bed respectively. θ_c is a function of the grain Reynolds number (Sumer and Fredsøe, 2002, p.10) and it is approximately 0.06 in this study.

The theoretical expression for the friction factor for very large and very small relative bed roughness (Fredsøe and Deigaard, 1992) is given by

$$f = \begin{cases} 0.04\left(\frac{a}{k_N}\right)^{-\frac{1}{4}} & if\ \frac{a}{k_N} > 50 \\ 0.4\left(\frac{a}{k_N}\right)^{-\frac{3}{4}} & if\ \frac{a}{k_N} < 50 \end{cases} \tag{5}$$

where k_N is the Nikurads roughness (around $2.5d_{n50}$), and $a = u_b{*}T/2\pi$, u_b is the instantaneous free stream horizontal wave velocity close to the bed and T is the incident wave period. The more generalized explicit formulas for the friction factor $f = \exp\left[7.02\left(\frac{k_N/30}{a}\right)^{0.078} - 8.82\right]$ *for* $10^{-2} < \frac{k_N/30}{a} < 5$ and $f = \exp\left[5.61\left(\frac{k_N/30}{a}\right)^{0.109} - 7.30\right]$ *for* $10^{-4} < \frac{k_N/30}{a} < 10^{-2}$ have 1% accuracy in comparison with the exact implicit formula (Madsen, 1994; Zou, 2004).

2.3. Morphological model

2.3.1. Partial cell technique

Fig. 1 provides an overview of the finite difference meshes and cell classifications in the model. The free surface is captured with the Volume of Fluid (VoF) method proposed by Youngs (1982), where the interface was approximated by a straight-line segment in each cell, but the line could be oriented arbitrarily with respect to the coordinate axis (Fig. 1). The orientation of the line is determined by the normal to the interface, which is found by considering the average value of void fraction in both the cell under consideration and neighbouring cells. The partial cell technique is applied to the water-soil interface. Partial cell treatment partially blocks the cell face and cell itself according to the real geometry of the boundary.

Since the interface in a cell is arbitrarily oriented in Youngs (1982) method, the openness of the cell face, $ar_{i,j}$, defined as the ratio of the fluid part to the vertical length of the cell, is more useful to describe cell properties (Fig. 1). The bed level in cell i,j, $z_{b,i}$, is related to $ar_{i,j}$ as follows:

$$ar_{i,j} = \frac{y_{j+1} - z_{b,i}}{y_{j+1} - y_j} \tag{6}$$

The present model uses the parameter $z_{b,i}$, which is independent of the vertical cell index, to represent the bed level height. $z_{b,i}$ is updated at each time step and consequently the new $z_{b,i}$ and $z_{b,i-1}$ is then used to update

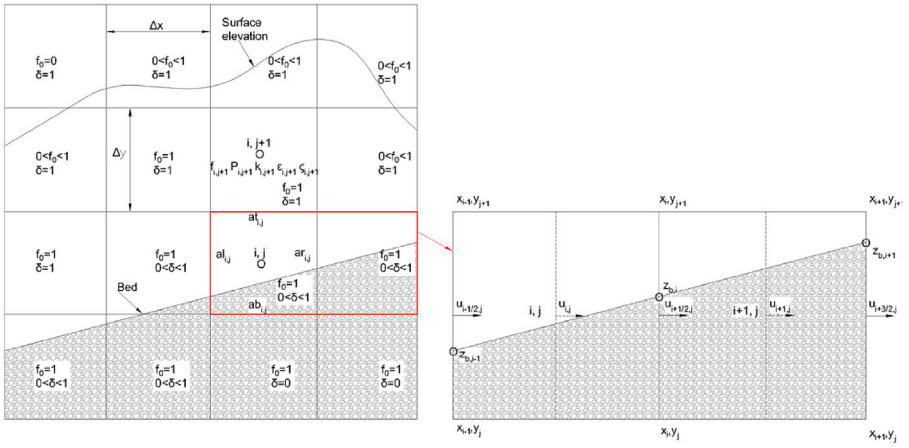

Fig. 1. (Left) Finite difference meshes and cell classifications in the present model (c.f. Peng, 2010) and (Right) sketch of cell adjacent to the water-soil interface for the present model: *i, j* are cell indexes; $Z_{b,i}$ is the bottom level; Δx_i is the cell length in horizontal coordinate, while Δy_j is the cell length in vertical coordinate; P_{ij}, k_{ij}, ϵ_{ij} and ζ_{ij} are the pressure, the turbulence kinetic energy, the turbulence dissipation rate and the viscosity at the cell center, respectively. Here, f_0 is the Volume of Fluid (VOF) function (the volume fraction occupied by the fluid) to capture the free surface, while δ is the Volumn of Soil (VOS) function (the volume fraction occupied by the soil) in analogy to VOF to capture the soil-water interface, $u_{i,j}$ are the horizontal velocity at the cell center; $at_{i,j}$, $ab_{i,j}$, $al_{i,j}$ and $ar_{i,j}$ are the ratio of fluid part to the vertical length of the cell at the top, bottom, left and right sides of the cell; $x_{i,j}$ and $y_{i,j}$ stand for the coordinates of the cell *i,j*.

the openness parameters, $at_{i,j}$, $ab_{i,j}$, $al_{i,j}$ and $ar_{i,j}$ in the cell *i, j*.

Based on the Forward in Time Upwind in Space numerical scheme, Eq. (1) could be differentiated as below (c.f. Fig. 1):

$$\frac{q(t)_{i+1} - q(t)_i}{(x_{i+1} - x_{i-1})/2} = -(1-n)^* \frac{z_{b,i+1/2}(t+\Delta t) - z_{b,i+1/2}(t)}{\Delta t} \tag{7}$$

where $q(t)$ is given by Eq. (2), and ub equals the mean of $u_{i-1/2,j}$ and $u_{i+1/2,j}$, one cell above the partial cell.

The bed profile is reconstructed through the updated cell face openness parameter, $ar_{i,j}$, which could be obtained from the new $z_{b,i}$. Details are given in the next sections. To avoid shock wave and singularity of fluid velocity after the bed level updating, a constraint has been applied in the computation: if the accumulated change in the bed level exceeds 20% of the deep water wave height *Hs*, reset it to $z_{b,i} = z_{b,i,old} + 20\%^* Hs$, where $z_{b,i}$ is new bed level, $z_{b,i,old}$ is old bed level and *Hs* is the deep-water wave height. Here 20% is chosen after trial and error.

2.3.2. Sand-slide model

The sand-slide model of Liang and Cheng (2005) is modified to improve the mass conservation of bed materials and then used to resolve the avalanching process and the five-point Gaussian averaging is applied to the newly updated bed levels to smooth out the small-scale bed features.

If the computed local bed slope between two neighbouring nodes is larger than the angle of repose, i.e., $\left|\frac{\partial z}{\partial x}\right| > \varphi$, the slumping of sandy material will occur due to the gravity and this is also called avalanching. In order to resolve the slumping of sandy materials, a new sand-slide model was developed in this study. This model is an extension of the sand-slide model by Liang and Cheng (2005) by improving the mass conservation of bed material. In addition, unrealistic bed shapes such as sharp corners sometimes occur and may affect the numerical stability of the morphological model. Since the main bed feature is the focus of the present study, it is justifiable to smooth out the small sharp corners and ripples regardless whether their presence is due to physical or numerical reasons.

If the bed slope is larger than the angle of repose, the new sand-slide model is implemented using the following procedure: firstly, rotate the local bed slope in the current cell (i,j) relative to the mid-point between the two adjacent nodes (dark dashed line) until the bed slope is reduced to the angle of repose (blue dash-dot line); secondly, decrease the bed level but maintain the same bed slope in the current cell so that the total mass of sediment within the current cell and neighbouring cells is conserved; thirdly, apply a five-point Gaussian averaging to the newly updated bed levels. Fig. 2 demonstrates the first two steps of the sand-slide model.

A set of formulae for the bed level updating calculation are given in the following in a step by step fashion as the updating processes may involve more than one neighbouring cell.

2.3.2.1. Step 1: updating at the current cell. Symmetrically rotate the local bed slope relative to the mid-point between the two nodes in the current cell until it is equal to the angle of repose.

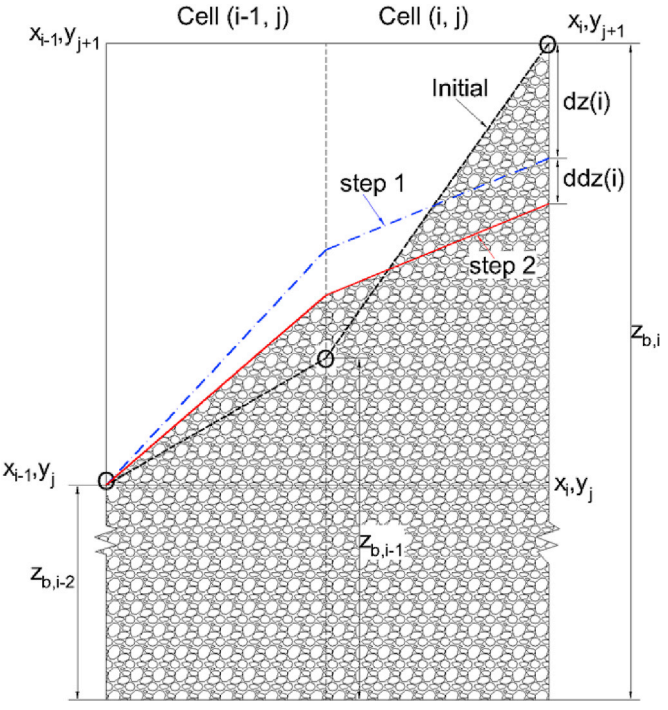

Fig. 2. Diagram of the modified sand-slide model. Dark long dashed line: original bed; blue short dash-dot line: interim bed (only consider the current cell); red solid line: final bed (take into account of the neighbouring cell). (For interpretation of the references to colour in this figure legend, the reader is referred to the web version of this article.)

$$dz(i) = \begin{cases} \dfrac{z_{b,i} - z_{b,i-1} - \tan\varphi^* dx_i}{2} & \text{if } z_{b,i} >= z_{b,i-1} \\ \dfrac{z_{b,i} - z_{b,i-1} + \tan\varphi^* dx_i}{2} & \text{if } z_{b,i} < z_{b,i-1} \end{cases} \quad (8)$$

where $z_{b,i}$ is the bed level on the right side of cell (i, j), $z_{b,i-1}$ is the bed level on the left side of cell (i, j), dx_i is the width of cell (i, j), and φ is the angle of repose. In this study, $\varphi = 31^\circ$ was adopted, following Gislason et al., (2009a, b).

Roelvink et al. (2010) proposed to limit the rate of change of bed level to less than 0.05 *m/s* to prevent the generation of large shock waves (Δt is time step of bed updating in this study). The bed level change within one time step is thus given by:

$$dz(i) = \min(dz(i), 0.05\Delta t), \frac{\partial z}{\partial x} > 0 \quad (9)$$

$$dz(i) = \max(-dz(i), -0.05\Delta t), \frac{\partial z}{\partial x} < 0 \quad (10)$$

2.3.2.2. Step 2: updating at the neighbouring cells. It is worth pointing out that the updated bed slope in the neighbouring cell (i-1, j) may be larger than the angle of repose, and therefore the sand-slide model application has to be extended to the next neighbouring cells, such as cell (i-2, j).

$$ddz(i) = \frac{dx_{i-1}{}^* dz(i)}{dx_i + dx_{i-1}} \quad (11)$$

$$z_{b,i} = z_{b,i,old} - (dz(i) - ddz(i)) \quad (12)$$

$$z_{b,i-1} = z_{b,i-1,old} + (dz(i) - ddz(i)) \quad (13)$$

2.3.2.3. Step 3: Gaussian averaging. A five-point Gaussian averaging is applied to the newly updated bed levels to smooth out the small-scale bed features to maintain the stability of numerical calculations.

$$z_{b,i} = 0.1z_{b,i-2} + 0.2z_{b,i-1} + 0.4z_{b,i} + 0.2z_{b,i+1} + 0.1z_{b,i+2} \quad (14)$$

2.3.3. Cells updating

In the present model, cells are characterized by three openness parameters: the fraction of fluid occupying the cell, $ac_{i,j}$; the fraction of fluid occupying the right side of the cell, $ar_{i,j}$, and the fraction of fluid occupying the top side of the cell, $at_{i,j}$. The bed cell index, ibed(i), can be obtained by:

$$ibed(i) = j \quad if \quad y(j-1) < z_{b,i} < = y(j) \quad (15)$$

Based on the difference between $z_{b,i}$ and $z_{b,i-1}$, we can categorize the cell updating into three scenarios as shown in Fig. 3. We update the openness parameters of the cell in two steps: firstly, employ the new $z_{b,i}$ to update $ac_{i,j}$, $ar_{i,j}$, $ab_{i,j}$ and $at_{i,j}$ for the cells at the water-soil interface; secondly, adjust the newly changed cells outside of water-soil interface cells that moves from soil to fluid or from fluid to soil. After these two steps, the cell openness characteristics are all updated and can be used for the calculations by the hydrodynamic model at the next time step.

2.4. Time step criteria

The standard von Neumann stability analysis was employed to obtain the stability criteria for the linear approximation of the hydrodynamic model (Lin and Liu, 1998). The time step Δt_m for the morphology is chosen to be larger than the time step Δt_h for the hydrodynamics because the time scale of the bed profile evolution is larger than that of the flow. It is expected that the time step for morphology Δt_m is small at the initial stage of the scour formation and becomes larger later as the scour process slows down. Therefore, to ensure a convergence toward a steady scour pattern, the morphological time step Δt_m should satisfy the criterion Eq. (16) as the morphology model used the Forward in Time Centered in Space (FTCS) finite difference scheme (Abbott and Basco, 1989):

$$\Delta t_m \leq 0.5 \frac{(\Delta x_{i,j})^2}{\varepsilon_s q_{\max}} \quad (16)$$

where q is the onshore and offshore sediment transport rate and ε_s has a constant value of 2.0 as proposed by Watanabe et al. (1994).

3. Model setup

To investigate the effects of wave breaking and beach slope on toe scour in front of vertical walls, and to validate the efficiency of partial cell technique, we conducted the following two types of wave-structure-soil interaction studies: (1) a standing wave with a vertical wall on a flat bottom; (2) a random wave with a vertical wall on a 1:30 sloping sandy beach. The first study is used to demonstrate the capability of the present model to resolve the hydrodynamics over a flat bottom in front of a vertical wall and the subsequent sediment transport and morphological change. The second study is used to investigate the effect of wave

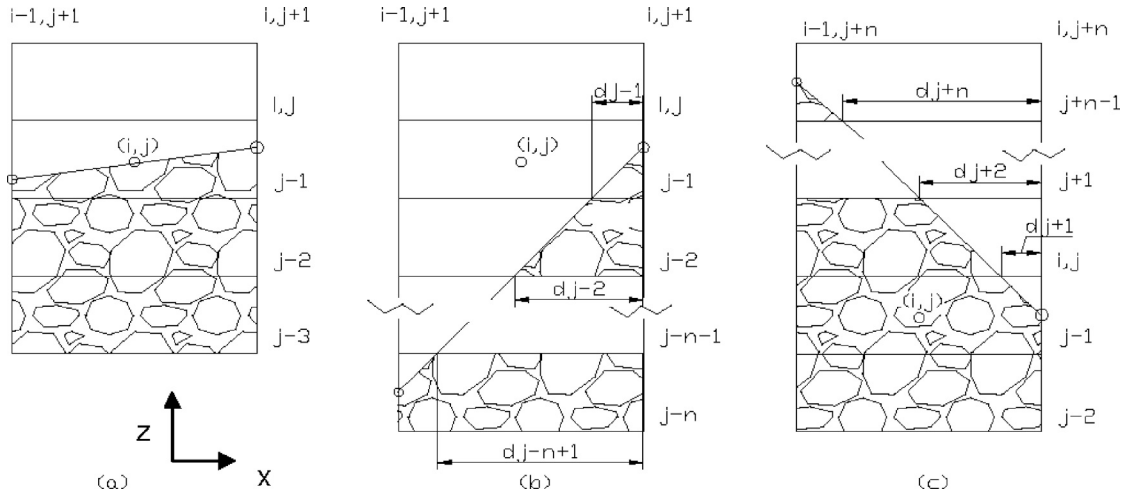

Fig. 3. Three scenarios of bed level difference in the adjacent cells occur during cell updating based on newly updated bed level $z_{b,i}$. d_j is the length of soil part in cells at y_j, (a) the bed intersects the left and right cell face of the same cell; (b) the bed intersects the left and right cell face of different cells with $z_{b,i} > z_{b,i-1}$; (c) the bed intersects the left and right cell face of different cells with $z_{b,i} < z_{b,i-1}$.

breaking and beach slope on the beach profile and toe scour in front of a vertical wall.

3.1. Flat bottom

The RANS-VOF hydrodynamics model in combination with sediment transport and morphological models are set up to simulate the laboratory experiment test L1 described in Table 1 of Gislason et al. (2009a, b) with the same flow and sediment parameters: Acrylic sediment, with the size $d_{n50} = 0.44$ mm, with the specific gravity of grains $s = \rho s/\rho = 1.13$, the fall velocity of grains $ws = 2$ *cm/s* and the angle of repose $\varphi = 31^{\circ}$.

Numerical model setup is illustrated in Fig. 4. In this study, the vertical wall at the far right is assumed as an impermeable obstacle, thus, no flux there. In order to minimize the reflected wave, an internal wave maker was employed and placed at around 4 wavelengths (wavelength is around 3.3 *m*) away from the vertical wall. A spongy layer was placed from x = −20 *m* to x = −14 *m* to absorb the reflecting waves. The incoming wave conditions are: wave height H = 0.02 *m*, wave period T = 2.0 s, wave length L = 3.3 *m*, water depth h = 0.31 *m*.

Four grid resolutions have been used to examine the convergence of the model meshes. Table 1 summarizes the model implementation for these four grid sizes. In order to resolve the boundary layer, ideally the grid size near the bed shall be as small as possible. However, the relative fixed ratio of horizontal to vertical grid size required for maintaining the model stability leads to a formidable computational workload. The grid 800*251 takes a minimum grid size of 5e-4 *m* in the vertical coordinate to resolve the boundary layer, as this grid size is comparable to the theoretical laminar boundary layer thickness, the Stokes length, of around 5.642e-4 *m*, according to the equation $\delta_1 = \sqrt{2\nu/\omega}$, where ν is the kinematic viscosity and ω is the angular frequency. Outside the boundary layer, the vertical grid size increases from 5e-4 *m* to 5e-3 *m*. The horizontal grid size is around 2.5 *cm*, which is sufficient enough to resolve the wave with a wavelength around 3.3 *m*. The thickness of wave turbulent boundary layer is given by $K*u_*/\omega$, where K = 0.4 is the von Karman constant, u_* is the friction velocity= $(0.5*f*u_b^2)^{1/2}$ (Zou, 2002). Following Gislason et al. (2009a, b), we used the Stokes length as a first estimate of the boundary layer thickness.

Fig. 5 shows the comparisons of model predicted flow velocities at 2 *m* away from the vertical wall, using four different grid resolutions described in Table 1. The magnitude of the instantaneous horizontal velocity increases with the horizontal grid size, though the model results for grid 800*251 and grid 2000*251 are almost identical. The negative vertical coordinates are related to the ghost cells due to the staggered grids used in the present model. The purpose of these ghost cells is to enable the full central-difference derivative calculations throughout the entire computational domain without any special treatment.

By averaging the instantaneous velocities over 10 wave cycles, it is interesting to observe the reversed mean flow horizontal velocity direction near the bottom for the grids 800*251 and 2000*251, which are not present for the coarser grids 400*62 and 400*125 (Fig. 5). The reversed mean flow velocity direction near the bottom is consistent with the double cell theory of standing wave streaming in front of a vertical wall (Sumer and Fredsøe, 2000 or Fig. 8). For the instantaneous vertical velocity, all four grid sizes gave converged results. There is a negligible mean vertical velocity at 2 *m* (around 0.6 wavelength) away from the seawall.

Based on above grid resolution sensitivity test, the grid 800*251 will be employed in this study by considering both accuracy and computational time.

Table 1
Summary of four grid resolutions and CPU.

Grid No.	Horizontal resolution [*m*]		Vertical resolution [*m*]		CPU wall time (30 waves)
	Min	Max	Min	Max	2G Hz and 4G memory
400*62	0.05	0.05	0.002	0.02	3.5 h
400*125	0.05	0.05	0.001	0.01	6 h
800*251	0.025	0.025	0.0005	0.005	24 h
2000*251	0.01	0.01	0.0005	0.005	84 h

3.2. Sloping bed

The toe scour in front of a vertical wall on a sloping bottom has also been investigated. The sloping beach decreases the water depths towards the vertical wall, leading to wave shoaling and potential wave breaking. The relatively shallow water depth also increases the wave energy dissipation due to bottom friction.

The model was setup in the same way (Fig. 6) as the toe scour experiments of random waves over a sloping bed by Sutherland et al. (2006). The model-measurement comparisons were used to investigate the toe scour process over a sandy beach with a 1:30 slope in front of a vertical wall, with a particular attention to the effect of wave breaking and relative water depth.

The vertical wall is located at x = 28 *m* and the sandy beach has a 1:30 slope. The horizontal grid size is 0.05 *m*, which is sufficient to resolve waves with a wavelength of at least 4.7 *m*. The vertical grid size is 0.01 *m* around the surface elevations and the mobile bed and 0.02 *m* at the other locations. Random waves are generated by the wave-maker at x = 0 *m* using the JONSWAP spectrum with a peak enhancement factor of 3.3. To avoid excessive computations but maintain the numerical stability, the second-order wave generation and absorption wave maker described by Torres-Freyermuth et al. (2010) instead of the internal wave maker, was employed and placed at x = 0 *m*, in order to eliminate the effect of reflected waves on wave generation.

The present model is validated with the physical tests by Sutherland et al. (2006). Table 2 shows a summary of the key wave parameters for the selected 3 model runs as a demonstration of the capability of the present model.

The sediment transport model used the same sediment parameters as those in Sutherland et al. (2006). The mobile sediment layer is located within 5 *m* from the vertical wall. The 50^{th} percentile grain diameter is 0.111 *mm*, and the specific gravity of grains is 2.65. The sediment model starts after 10 wave cycles in order to obtain relatively stable hydrodynamics. The sediment model uses a time step of 0.01 *s*, while the morphology model employs a time step of 2 *s*. As mentioned in Section 2.4, the different time steps for sediment transport model and morphology model are due to much larger time scale of morphology changes than hydrodynamics changes.

4. Model-data comparison

4.1. Scour in front of a vertical wall over a flat bottom

4.1.1. Wave kinematics

When the incoming waves encounter the vertical wall, most of wave energy will be reflected back. Part of energy will be dissipated through the turbulence and bottom friction. After several wave periods, the standing waves would be formed, with a series of nodes and anti-nodes, where the surface elevation remains constant with time. The water surface oscillates up and down around the still water level between anti-nodes and nodes. Next the modelled surface elevation and orbital velocities will be validated by the theory.

The analytical solution for the surface elevation of the standing waves could be derived from the Airy wave theory as below:

$$\eta_1(x,t) = a\cdot\cos(kx - \omega t) \tag{17}$$

$$\eta_2(x,t) = a\cdot\cos(kx + \omega t) \tag{18}$$

$$\eta(x,t) = \eta_1(x,t) + \eta_2(x,t) = 2a\cdot\cos(kx)\cdot\cos(\omega t) \tag{19}$$

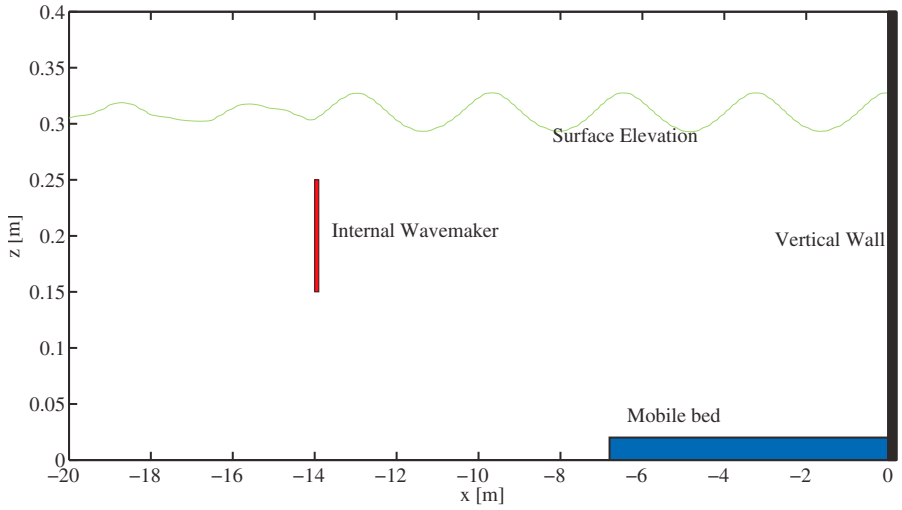

Fig. 4. Schematization of numerical model set-up for standing waves on a flat bed.

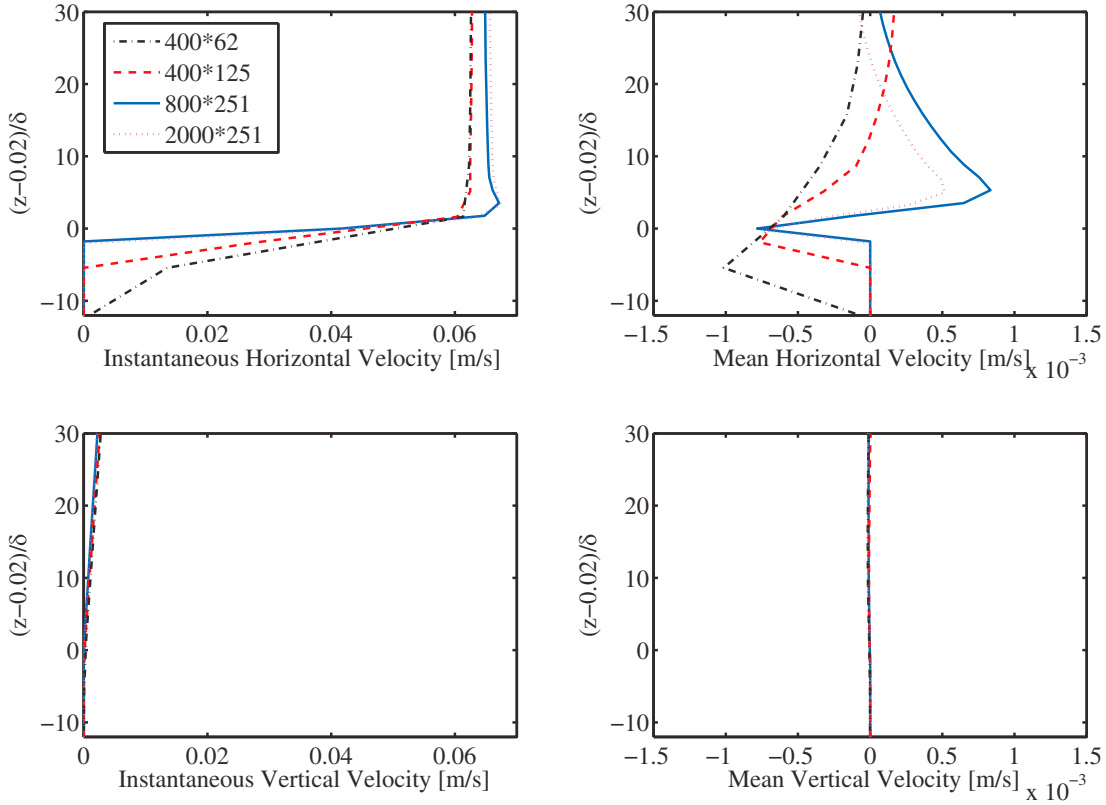

Fig. 5. Model grid resolution convergence test, $\delta_1 = \sqrt{2\nu/\omega}$ is the theoretical laminar boundary layer thickness of 5.642e-4 *m*. The velocities shown were obtained at 2 *m* (around 0.6 wave length) away from the Seawall. Here the sediment layer is 0.02 m thick above the origin of the axis, thus we deduct 0.02 m from z to represent the vertical coordinate in the figure.

The horizontal and vertical velocity could be derived from the velocity potential as below:

$$u(x,t) = \omega{\cdot}a{\cdot}\frac{\cosh(kz)}{\sinh(kh)}{\cdot}\cos(kx-\omega t) - \omega{\cdot}a{\cdot}\frac{\cosh(kz)}{\sinh(kh)}{\cdot}\cos(kx+\omega t)$$
$$= 2\omega{\cdot}a{\cdot}\frac{\cosh(kz)}{\sinh(kh)}\sin(kx)\sin(\omega t) \tag{20}$$

$$v(x,t) = \omega{\cdot}a{\cdot}\frac{\sinh(kz)}{\sinh(kh)}{\cdot}\sin(kx-\omega t) - \omega{\cdot}a{\cdot}\frac{\sinh(kz)}{\sinh(kh)}{\cdot}\sin(kx+\omega t)$$
$$= -2\omega{\cdot}a{\cdot}\frac{\sinh(kz)}{\sinh(kh)}\cos(kx)\sin(\omega t) \tag{21}$$

where σ and ω are the angular frequency, a the wave amplitude, and k the wave number.

Fig. 7 shows the comparisons of standing wave velocities predicted by the present numerical model and the Airy wave theory. The origin of the velocity plots is at the bottom of the model domain, including the 2 cm-

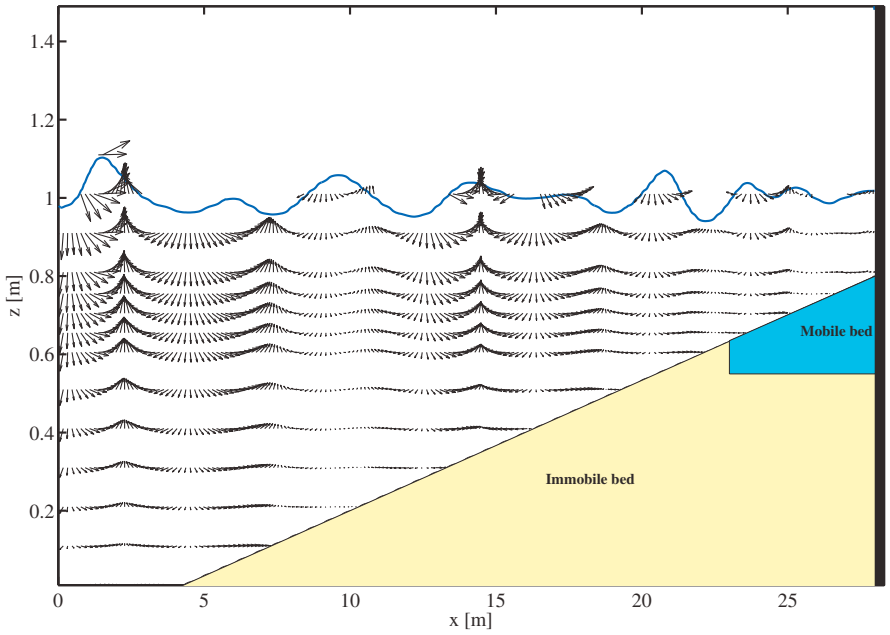

Fig. 6. Numerical model setup and a snapshot of surface elevation and flow field. The Seawall is at $x = 28$ *m*.

Table 2
Wave height, wave period, and water depth at the inlet and at the toe of the wall for selected model runs for toe scour on a sloping beach.

Case No.	H_s (m)	T_p (s)	h_0 (m)	h_{toe} (m)	Experiment test No. by Sutherland et al. (2006)
1	0.2	1.87	1.25	0.4	Case 9
2	0.2	3.24	0.95	0.1	Case 12
3	0.2	1.87	1.0	0.2	Case 2

thick sediment layer, leading to zero orbital velocity at around z = 2 cm. For standing wave at Anti-node, the modelled horizontal velocity is close to zero. The modelled vertical velocities agree well with the theory. For standing wave at Node, the modelled vertical velocity is close to zero. The modelled horizontal velocities agree well with the theory. The discrepancies between the model and theory are due to the partially instead of full standing waves generated by the model, caused by the small amount of reflected waves from the wave-maker and wave energy dissipation.

For both cases, the model and theory predicted surface elevations are in good agreement with each other.

4.1.2. Steady streaming

The oscillating motion of a fluid may generate a slow Eulerian mean flow related to inertia effects, known as 'steady streaming' (Riley, 2001). It is related to the horizontal gradient of the wave phase or wave amplitude (Batchelor, 1967). A phase gradient typically corresponds to a gravity wave travelling over a flat bottom; here the streaming flow is uniform and consists of a near-bed jet in the wave direction (Longuet-Higgins, 1953; Ünlüata and Mei, 1970; Craik, 1982).

As shown in Fig. 8, once the standing wave over a flat bed is formed, it leads to the alternating streaming velocity directions in the horizontal axis, where the streaming velocity is the largest between nodes and anti-nodes, and streaming velocity is close to zero at the anti-nodes and nodes (Sumer and Fredsøe, 2000). The steady streaming plays an important role in the sediment transport over a flat bed. As illustrated by Fig. 8, the streaming velocity in the opposite direction at the top of the boundary layer creates the well-known double recirculating cell pattern, and the sediment on the bed responds to these recirculating cells.

Distribution of instantaneous water surface at $t = 60$ *s* can be found in Fig. 4. The spatial variation of surface elevations illustrates alternating anti-nodes and nodes with the wavelength of around 3.3 *m*, which is consistent with theory prediction of anti-nodes at $x = nL$ and (n+1/2)L and nodes at (n+1/4)L and (n+3/4)L, while L is wave length, n is the integer.

In this study, the steady streaming velocity was obtained by averaging over 10 consecutive waves, for incoming wave height $H = 0.02$ *m*, wave period $T = 2.0$ *s*, wave length $L = 3.3$ *m* and water depth $h = 0.31$ *m*. Fig. 9 illustrates the distribution of steady streaming velocity magnitude and corresponding directions in front of the vertical wall. Fig. 9 displays double recirculating cells generated by the standing wave, similar to Gislason et al. (2009b) and Fig. 8, showing the alternating velocity directions in the horizontal axis between anti-nodes and nodes.

4.1.3. Morphological changes and scour

Since these double circulating cells are essential to sediment transport and are well reproduced by the present model on a flat bottom, this model will be used to study the toe scour in front of a vertical wall with a flat bottom next. Similar to the experiment, a sediment layer (6.6 *m* in length and 0.02 *m* in thickness) was incorporated into the numerical model, so that the water depth change from 0.31 m at the wave-maker to 0.29 *m* near the vertical wall (Fig. 4).

The sediment transport model use the same sediment parameters as those in Gislason et al. (2009a, b). The sediment layer is located within 2.4 *m* away from the vertical wall. The sediment layer has a thickness of 0.02 *m*. The 50^{th} percentile grain diameter is 0.44 *mm*, and the specific gravity of grains is 1.13. As discussed in Gislason et al. (2009a, b), the suspended load is not important in the morphological changes in the experiment and was neglected in their model. The sediment transport model starts after 10 wave cycles in order to obtain relatively stable hydrodynamics. The sediment model uses a time step of 0.01 *s*, while the morphology model employs a time step of 2 *s*. This is because the morphology changes are at a time scale much larger than the hydrodynamics changes.

After 300 wave cycles, the predicted bed profile is shown in Fig. 10. The measured bed profile in the experiments was digitized from Fig. 6 in Gislason et al. (2009a, b). The present model is capable to reproduce the alternating scour and deposition processes in front of a seawall on a flat bottom under regular waves as expected in theory. The observed scour

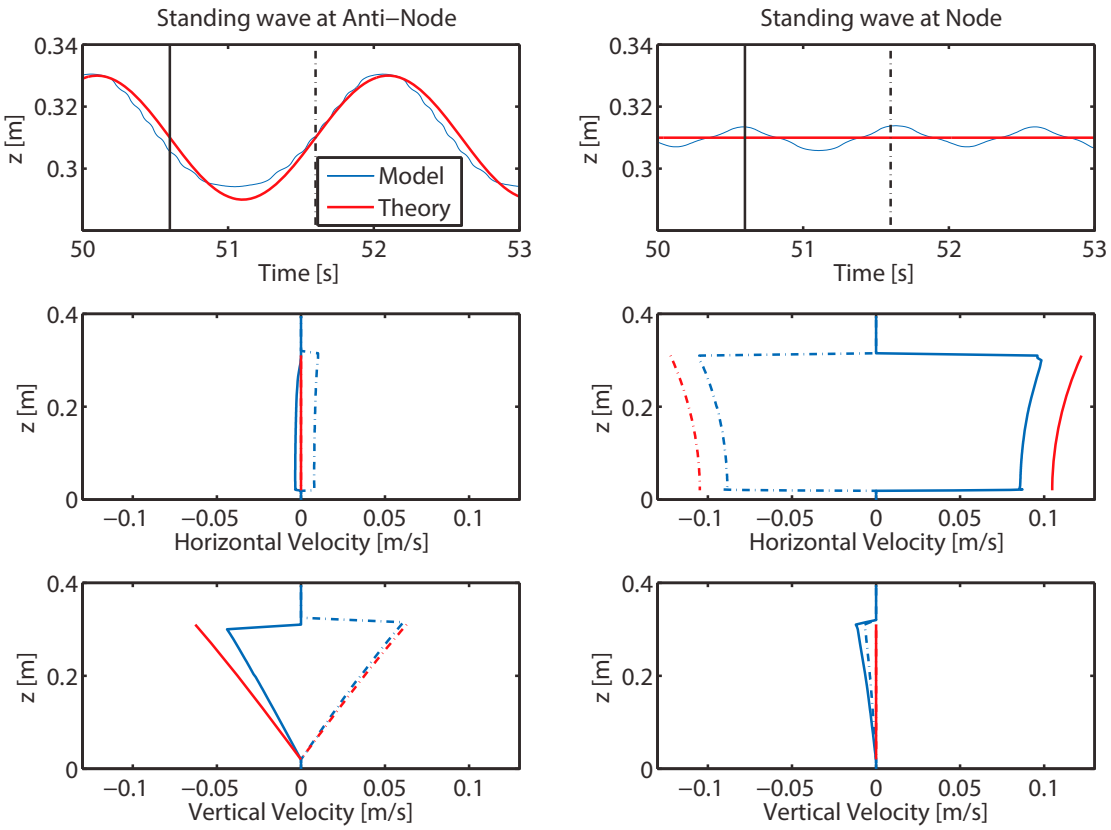

Fig. 7. Comparison of standing wave surface elevation (Upper) and horizontal (Middle) and vertical velocities (Lower) predicted by the present model (blue) and the Airy wave theory (red). Solid and dashed lines in the middle and lower panels stand for the horizontal and vertical velocities at the two different wave phases indicated by the vertical straight solid and dashed lines in the upper panel. (For interpretation of the references to colour in this figure legend, the reader is referred to the web version of this article.)

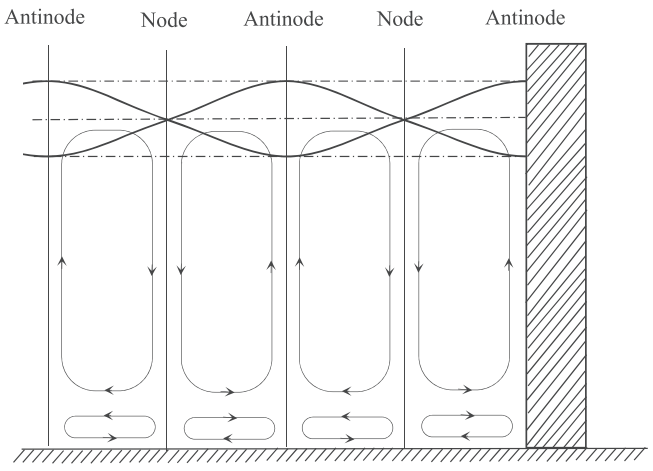

Fig. 8. Steady streaming over the flat bed in front of a vertical wall (modified from Sumer and Fredsøe, 2000).

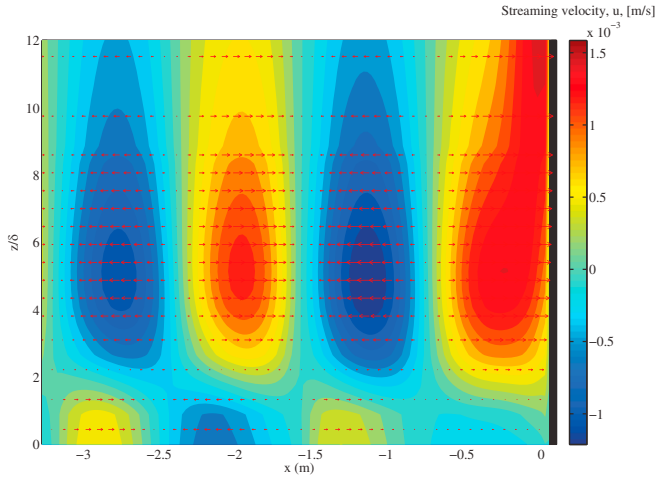

Fig. 9. Steady streaming velocity (colorbar) and its horizontal component (vectors), averaged over 50 consecutive waves, for incoming wave height $H = 0.02$ *m*, wave period $T = 2.0$ s, wave length $= 3.2$ *m* and water depth $h = 0.29$ m $\delta_1 = \sqrt{2\nu/\omega}$ is the theoretical laminar boundary layer thickness of 5.6e-4 *m*. The Seawall is at $x = 0$.

and deposition pattern relative to the node and antinode is also well captured by the model. The predicted equilibrium scour depth and bed profile are in good agreement with the experiment. Fig. 10 indicates that the toe scour occurs between the first node and the vertical wall, while the deposition occurs at the first node. This is because the first node is the convergence point for the near bed mean velocity (Fig. 8). The ripples appeared in the measurements are not captured due to the large morphology time step and Gaussian averaging in our model, they are, however, negligible as their magnitudes are relatively small.

4.2. *Scour in front of a vertical wall over a sloping beach*

4.2.1. *Relatively short wave and large toe water depth*

Random waves were generated from JONSWAP spectrum with a significant wave height $H_s = 0.2$ *m*, peak wave period $T_p = 1.87$ s, deep water depth $h_0 = 1.25$ *m* and water depth at the toe of the wall $h_{toe} = 0.4$ *m*. (Case 1 indicated in Table 2).

Fig. 11 represents the snapshots of velocities encountering the

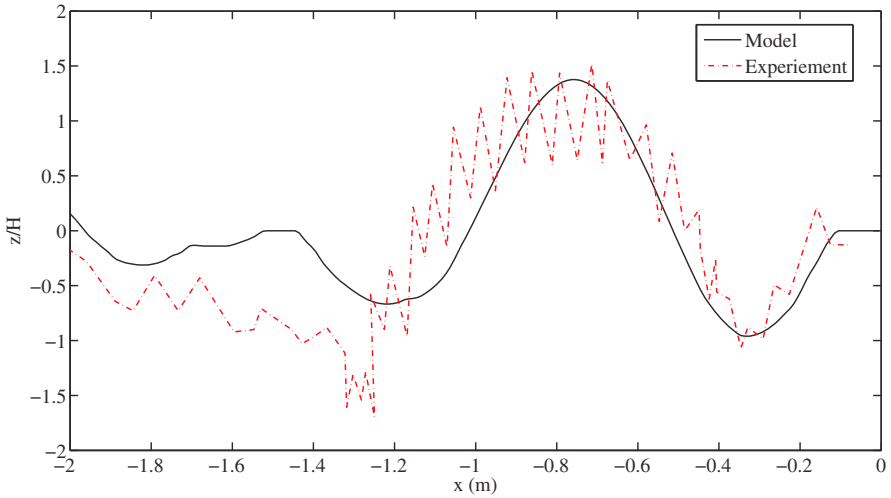

Fig. 10. Comparison of predicted scour and deposition by the present model and measurements by Gislason et al. (2009a, b). H is the incident wave height, and wave length is 3.3 m. Seawall is located at $x = 0$.

vertical wall. Due to the large water depth at the toe of the vertical wall, the incoming flow towards to the vertical wall is nearly uniformly distributed. Once it encounter the vertical wall, the wave direction is reversed. The magnitude of velocities decreases from the water surface to the bed, which contributes to the scour to some extent. This agrees with the theory of orbital velocities in the full water column. The near bottom velocity is not large enough to move significant amount of sediments within the mobile bed area, therefore, the scour and the deposition are relatively small.

Fig. 12 shows the hydrodynamics averaged over 50 wave cycles. The averaged velocity near the water line is considerably large, but not near the wall. In front of the vertical wall, there are eddies generated with near-bed streaming towards the wall. The incoming wave climbs and surges along the vertical wall. Once the surging wave jet turns around and falls into the water, it is carried away from the vertical wall by the undertow in the offshore direction. Therefore, the counter clock-wise eddies are formed. The reflected waves travel away from the vertical wall against the incoming flow. There is significant mean flow at the surface towards the wall and near the bed away from the wall. The turbulence kinetic energy represents the turbulence intensity, due to the turbulence and nonlinear wave interactions. There are limited wave breaking in this case as the magnitude of turbulence energy dissipation is small.

Fig. 13 shows that the bed profile change is small and undulated with alternating scour and deposition pattern. The near-bed undertow transports the sediment away from the vertical wall. However, as shown in Fig. 12, the counter clock-wise eddies in front of the vertical wall lead to near bed streaming towards the wall, and move the position of maximum scour depth away from the wall, rather than at the direct toe of the wall. This explains why the maximum scour occurs at $x = 27.6$ m instead of $x = 28$ m where toe of the vertical wall is. The present model reproduces the magnitude and position of scour well, but overestimates the magnitude of deposition.

Therefore, for this test case, scour is mainly induced by eddies in front

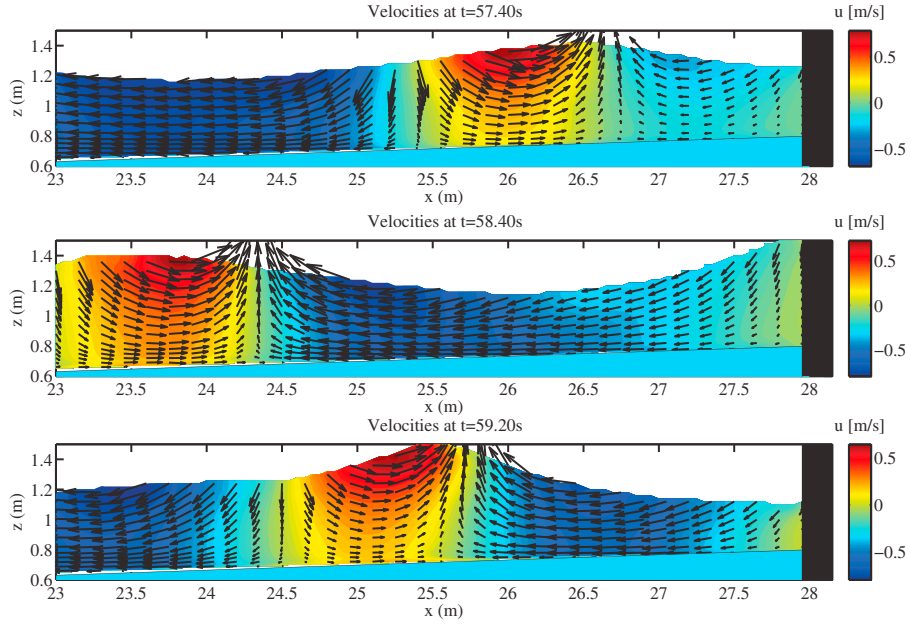

Fig. 11. Instantaneous velocity (vectors) and its horizontal component (color bar) for an irregular wave over a bed slope of 1:30, a significant wave height $H_s = 0.2$ m, peak wave period $T_p = 1.87$ s, deep water depth $h_0 = 1.25$ m and water depth at the toe of the wall $h_{toe} = 0.4$ m. (For interpretation of the references to colour in this figure legend, the reader is referred to the web version of this article.)

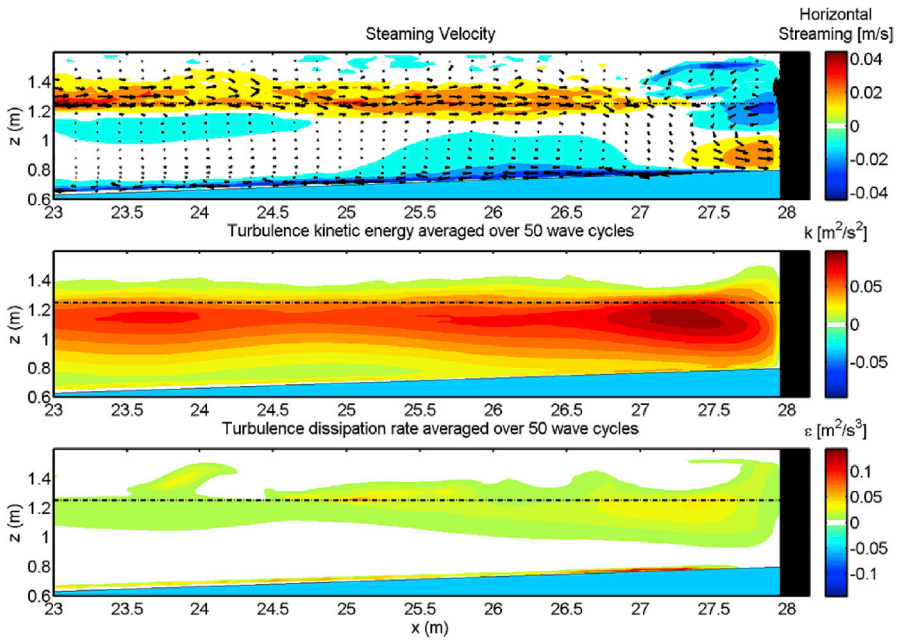

Fig. 12. Upper: Streaming velocity (vectors) and its horizontal component (color bar) by averaging over 50 wave cycles; Middle and Lower: turbulence kinetic energy and dissipation for an irregular wave over a bed slope of 1:30, a significant wave height $H_s = 0.2$ *m*, peak wave period $T_p = 1.87$ s, deep water depth $h_0 = 1.25$ *m* and water depth at the toe of the wall $h_{toe} = 0.4$ *m*. (For interpretation of the references to colour in this figure legend, the reader is referred to the web version of this article.)

of the wall and the partial standing waves adjacent to the wall.

4.2.2. Relative long wave and small toe water depth

Random waves were generated from JONSWAP spectrum with a significant wave height $H_s = 0.2$ *m*, peak wave period $T_p = 3.24$ s, deep water depth $h_0 = 0.95$ *m* and water depth at the toe of the wall $h_{toe} = 0.1$ *m* (case 2 indicated in Table 2).

Fig. 14 represents the velocity fields at the selected times. Waves start breaking around x = 27 *m* with the largest velocity at the plunging tongue which in turn leads to a strong, uniformly distributed incoming flow towards the vertical seawall. Once it hits the vertical wall, the wave plunges upon the face of the seawall and generates splashes upward and a strong jet downward, producing strong undertow and turbulence near the wall as shown in Fig. 15.

These phenomena can also be observed in Fig. 15, which shows the flow field averaged over 50 wave cycles. The strong streaming velocity appears near the still water line (water depth h = 0.95 m) towards the vertical wall and near the bed away from the wall. The dominant incoming streaming flow reaches the vertical wall, reflected back away from the vertical wall. This strong undertow transports the sediment particles offshore. Compared to case 1, this case has longer incoming waves travelling at a higher speed, and waves break at locations closer to the vertical wall, due to its relatively smaller wave steepness. The turbulence kinetic energy and dissipation rate is mainly due to the turbulence generated by the wave breaking. Wave breaking is a dominant process in this case as the magnitude of turbulence energy dissipation is large in front of the wall as indicated by Fig. 15.

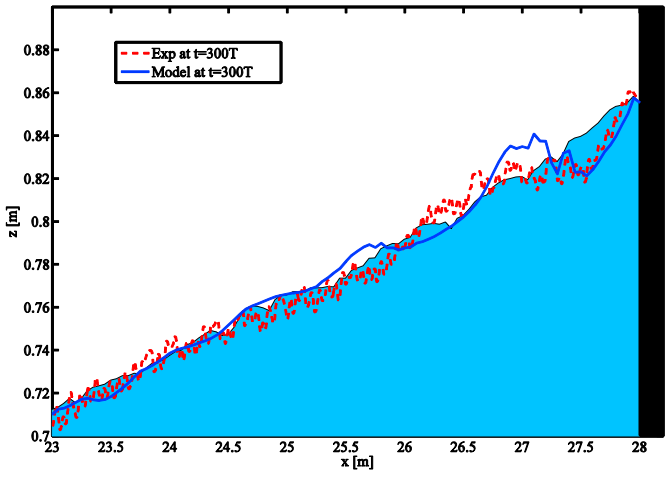

Fig. 13. Comparisons of predicted bed profile (blue solid line) and measurements (red dashed line) after 300 waves, for an irregular wave over a bed slope of 1:30, a significant wave height $H_s = 0.2$ *m*, peak wave period $T_p = 1.87$ s, deep water depth $h_0 = 1.25$ *m* and water depth at the toe of the wall $h_{toe} = 0.4$ *m*. (For interpretation of the references to colour in this figure legend, the reader is referred to the web version of this article.)

Fig. 16 shows the time evolution of turbulence kinetic energy, k, over a typical wave cycle. Results show that the turbulence kinetic energy, k, has large values around the wave break point when the flow pile up against the Seawall with large water depth at the toe; it then penetrates down into water column when the flow rush down backwards from the Seawall with a small water depth at the toe. When the k is averaged over 50 wave cycles (based on the incoming wave peak period of 3.24 s), the existence of downward penetrated k associated with small water depths leads to a large averaged k value slightly below the still water level (h = 0.95 m).

Fig. 17 shows that the beach profile evolves from the initially smooth profile to an undulating profile. There is a large scour area at the toe of the vertical wall followed by a small deposition area immediately seaward. The scour occurs directly at the toe of the vertical wall because there are no eddies in the front of the vertical wall to produce streaming towards the wall as shown in Fig. 12 for case 1. The near bottom streaming is directed offshore away from the wall over the whole computational domain. The small local water depth (0.1 *m*) results in a uniformly distributed velocity instead of counter clock-wise eddy observed in case 1. The position of the first node of partial standing waves is at around 0.8 *m* away from the wall, according to the local wavelength of around 3.2 *m*. This could explain why the deposition area is at 0.8 *m* away from the wall which the first node of partial standing waves from the wall, similar to that in Case 1. The predicted beach profile and scour and deposition pattern (blue solid line) agrees reasonably well with measurements (red dashed line). The predicted maximum scour depth

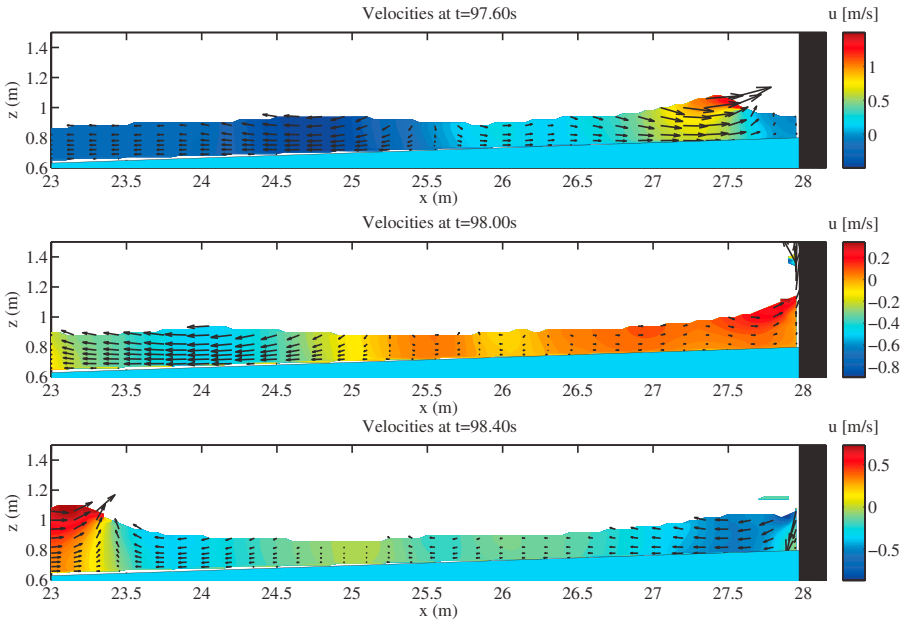

Fig. 14. Instantaneous flow velocity (vectors) and its horizontal component (color bar) for an irregular wave over a bed slope of 1:30, with a significant wave height $H_s = 0.2\ m$, peak wave period $T_p = 3.24$ s, deep water depth $h_0 = 0.95\ m$ and water depth at the toe of the wall $h_{toe} = 0.1\ m$. (For interpretation of the references to colour in this figure legend, the reader is referred to the web version of this article.)

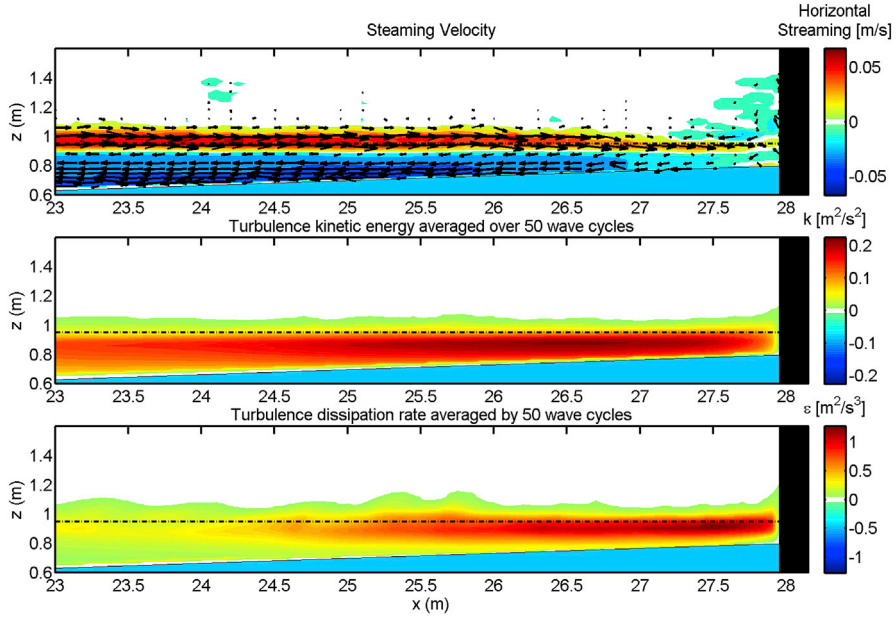

Fig. 15. Upper: Streaming velocity (vectors) and its horizontal component (color bar) by averaging over 50 wave cycles; Middle and Lower: turbulence kinetic energy and dissipation for an irregular wave over a bed slope of 1:30, with a significant wave height $H_s = 0.2\ m$, peak wave period $T_p = 3.24$ s, deep water depth $h_0 = 0.95\ m$ and water depth at the toe of the wall $h_{toe} = 0.1\ m$. (For interpretation of the references to colour in this figure legend, the reader is referred to the web version of this article.)

and deposition also agree well with the measurements.

For this case, the wave breaking just before the wall leads to the downward water jets towards the toe of the wall and large near bottom offshore current away from the wall. Scouring is attributed mainly to this near bottom offshore current generated by the breaking and the partial standing waves adjacent to the wall.

4.2.3. *Relatively long wave and intermediate toe water depth*

Random waves were generated from JONSWAP spectrum with a significant wave height $H_s = 0.2\ m$, wave period $T_p = 1.87$ s, deep water depth $h_0 = 1.0\ m$ and water depth at the toe of the wall $h_{toe} = 0.2\ m$ (case 3 indicated in Table 2).

Fig. 18 represents the snapshots of flow velocities in front of the vertical wall. The model results show that incoming waves break between x = 23 *m* and x = 25 *m*, leading to a strong flow at the wave crest towards the vertical wall. Due to the small water depth, the undertow and near bottom velocity is strong, resulting in the large scour depths and depositions.

Fig. 19 shows the flow field averaged over 50 wave cycles. The streaming velocity near the still water line is considerably larger than other locations but not so near the vertical wall, indicating that most wave energy has been dissipated due to wave breaking before reaching

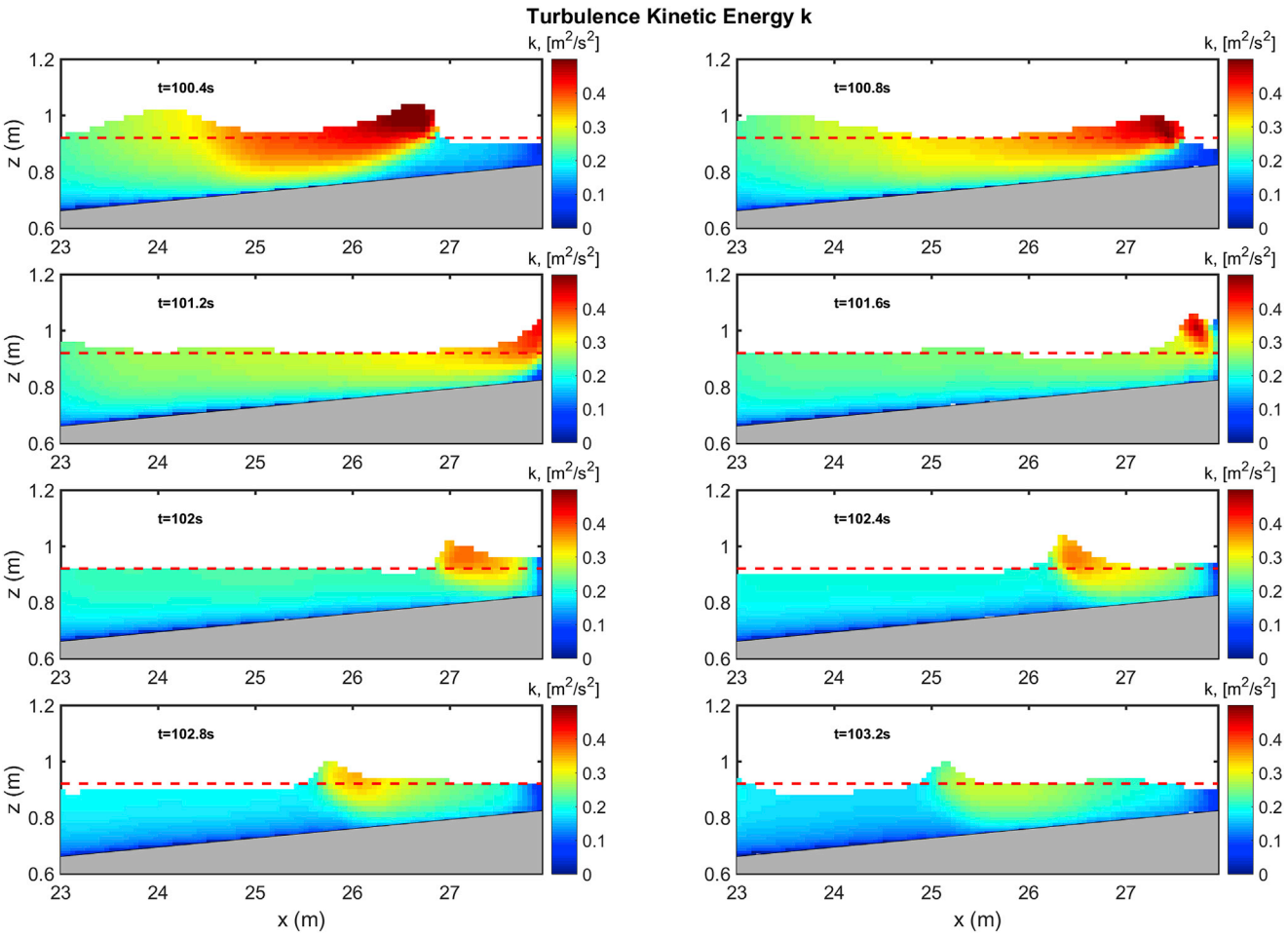

Fig. 16. Time evolution of turbulence kinetic energy, k, over a typical wave cycle for an irregular wave over a bed slope of 1:30, *with* a significant wave height $H_s = 0.2$ *m*, peak wave period $T_p = 3.24$ s, deep water depth $h_0 = 0.95$ *m* and water depth at the toe of the wall $h_{toe} = 0.1$ *m*. Red dashed line represents the still water level. (For interpretation of the references to colour in this figure legend, the reader is referred to the web version of this article.)

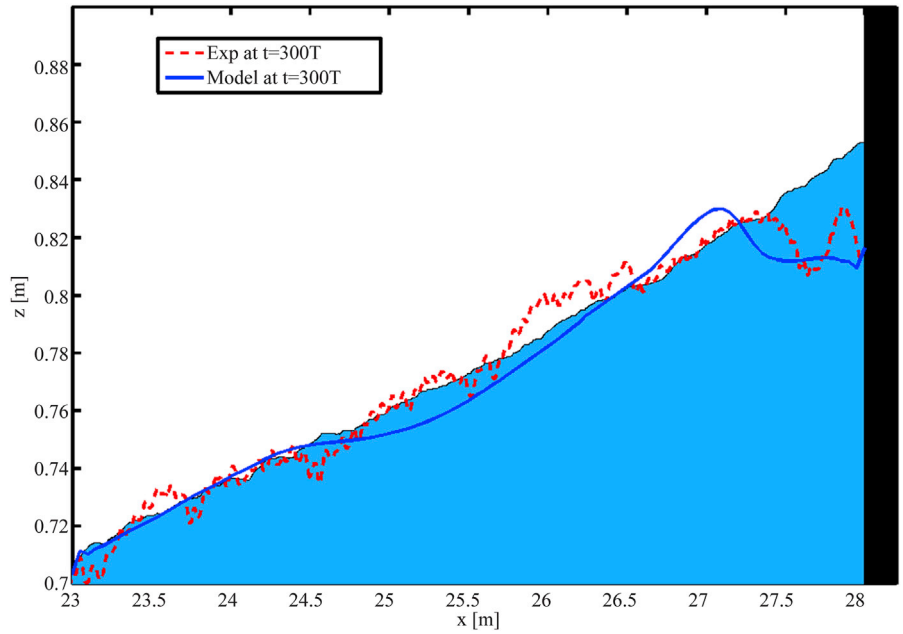

Fig. 17. Comparisons of predicted bed profiles by the present model and measurements, *with* a significant wave height $H_s = 0.2$ *m*, peak wave period $T_p = 3.24$ s, deep water depth $h_0 = 0.95$ *m* and water depth at the toe of the wall $h_{toe} = 0.1$ *m*. Seawall is at the end of the x-axis where $x = 28$ *m*.

the wall. This conjecture is supported by the turbulence kinetic energy and dissipation rate in the middle and bottom panels which show that significant dissipation occurs before the vertical wall. In front of the vertical wall, a counter clockwise vortex is present and generates a near-bed streaming towards the wall with smaller magnitude than that in Case 1.

As can be seen from Fig. 20, the predicted beach profile as well as the calculated maximum scour depth and deposition agrees well with the measurement. The initial beach profile is taken from the measurements. Comparison of Figs. 17 and 20 shows that the horizontal extent of the toe scour is smaller while the maximum deposition is larger for case 3 than that for case 2. According to the local wavelength of around 2.5 *m*, the position of the first node of partial standing waves away from the wall is at around 0.6 *m*. This could explain why the maximum scour occurs around 0.3 *m* away from the vertical wall, while the maximum deposition is at around 0.6 *m* away from the vertical wall.

For this case, wave breaking is of key importance in dissipating the incoming wave energy. Scouring is mainly induced by the partial standing waves adjacent to the wall and small counter clockwise streaming vortex in front of the wall.

5. Discussions

The model results of a standing wave over a flat bottom compare well with theory. The well-known double circulating cells are reproduced and the model shows the same alternating patterns as predicted by theory and previous studies. The predicted scour and deposition patterns over a flat bottom in front of a Seawall are in good agreement with the laboratory measurements.

For waves propagating over a sloping beach, the model results are in good agreement with the measurements for different incoming wave conditions and local water depths. The streaming velocity and wave bottom orbital velocity along the seabed are strongly dependent on the incident wave conditions, wave breaking types and locations. The wave breaking reduces the wave reflection and generates an offshore undertow current near the sea bed away from the wall so that the double-cell streaming circulation with alternating direction in case of flat bottom no longer exists. As a result, the alternating scour and deposition pattern for a flat bottom is not observed and the scour occurs mainly near the toe of the Seawall.

The aim of this study is to demonstrate the robustness of partial cell technique on structured grids to track the movement of the deforming water-soil interface, and subsequently improve the prediction of beach morphology change and toe scour in front of a coastal structure. By assuming the bedload transport is the dominant mode of sediment transport, we neglect the contribution of suspend sediment in our sediment transport model. This assumption is valid only if the near bed turbulent mixing is relatively small compared to the gravity for a given sediment size. For example, there is no wave breaking, or wave breaking induced turbulence does not penetrate deep enough to influence the sediment near the bottom. We should emphasize, however, that the novel concept of partial cell technique proposed here is applicable regardless if the sediment transport is dominated by bedload or suspended sediment or both.

The time averaged turbulence kinetic energy and dissipation rate in Figs. 12, 15, 16 and 19 in Section 3.2 indicate that the maximum turbulence are concentrated in the middle of the water column, rather than at the bottom. These results suggest that the suspended sediment may be present but is not a major factor in the beach morphological change and toe scour in these selected small to medium scale test cases. This explains why the present model that only considers the bedload transport, can capture the observed beach profile change and toe scour in these selected test cases. In the large scale experiments and field conditions, the suspended sediment is expected to play an important role in scour around a structure. The selected cases from the small and medium scale experiments may be bedload dominated due to the scaling effect and incoming wave conditions. Sumer and Fredsøe (2000) declared that most existing laboratory experiments on scour at a Seawall were performed at relatively small scales, therefore, dominated by bedload transport. Though Sutherland et al. (2006) intended to introduce suspended sediment transport in their experiments, they designed their test conditions based on the sediment fall velocity equation by Soulsby (1997) and wave conditions at the toe of the beach instead of the toe of the structure. Their experimental results imply the presence of suspended sediment but does not indicate that the suspended sediment plays a dominant role in toe scour during each of their test conditions.

Despite the relatively good performance of the present model for the selected test cases, this model is not appropriate when strong near bed

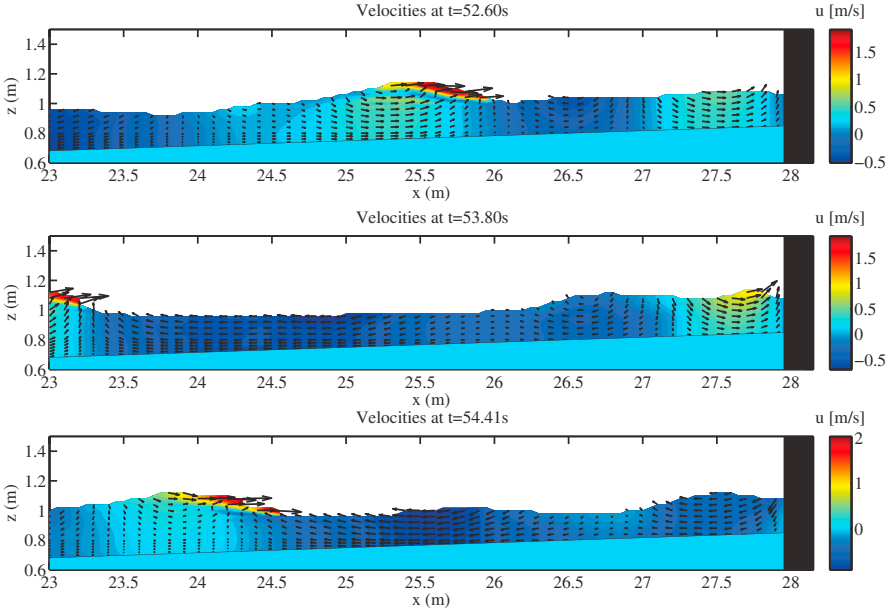

Fig. 18. Instantaneous velocity and its horizontal component (color bar) over a bed slope of 1:30, with a significant wave height $H_s = 0.2$ *m*, wave period $T_p = 1.87$ s, deep water depth $h_0 = 1.0$ *m* and water depth at the toe of the wall $h_{toe} = 0.2$ *m*. (For interpretation of the references to colour in this figure legend, the reader is referred to the web version of this article.)

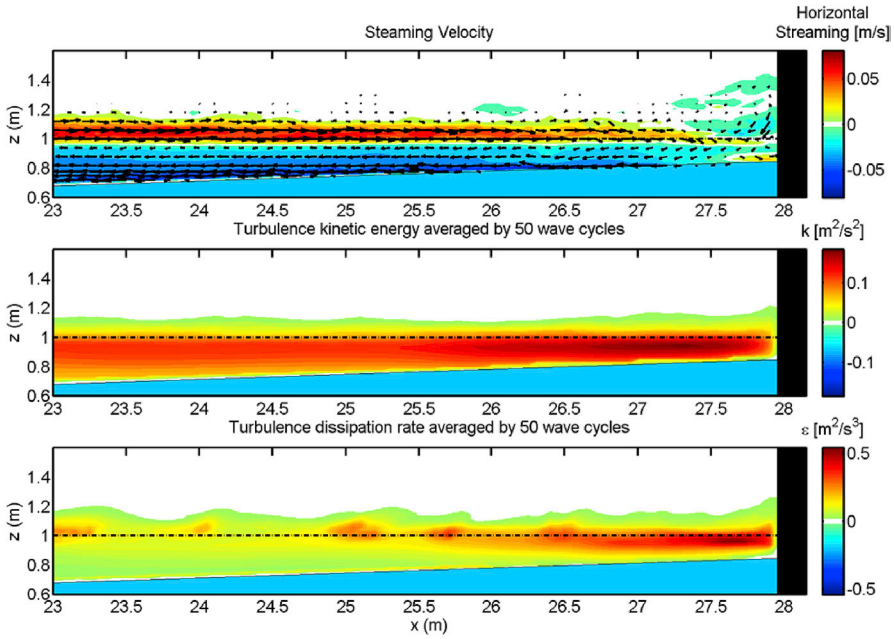

Fig. 19. (Upper) Streaming velocity and its horizontal component (color bar) by averaging over 50 wave cycles and (Middle and Lower) turbulence kinetic energy and dissipation rate over a bed slope of 1:30, with a significant wave height $H_s = 0.2\ m$, wave period $T_p = 1.87$ s, deep water depth $h_0 = 1.0\ m$ and water depth at the toe of the wall $h_{toe} = 0.2\ m$. (For interpretation of the references to colour in this figure legend, the reader is referred to the web version of this article.)

turbulence is induced by wave breaking. In the latter case both suspended and bedload sediment should be included in the sediment transport model. Although k-omega model is more accurate within the turbulent boundary layer, its accuracy degenerates towards the free surface. In this study, the breaking wave induced turbulence and undertow current is also important. The k-eps model is the most common turbulent model that can capture the wave-induced bottom boundary layer reasonably well. Thus we decided to use the k-eps model for the bedload dominant cases in this study. In the presence of significant suspended sediment, however, a k-omega or k-omega SST type turbulence model might be better choice since they can better resolve the turbulence throughout the boundary layer and solve the advection and diffusion equation of suspended sediment such as that in Hsu and Liu (2004) and Jacobsen et al. (2014b).

As discussed previously, wave hydrodynamics and morphodynamics in front of coastal structure are rapidly evolving and closely interlinked processes during storm events. The beach erosion and scour lead to a larger still water depth, therefore larger waves at the structure before breaking. Larger waves in turn lead to more beach lowering and scour, which creates a positive feedback that eventually undermines the structure (Zou and Reeve, 2009). Larger waves are expected to generate larger wave overtopping which may erode and damage the leeward face and crown of the coastal defence and destroy properties behind the defence (Pullen et al., 2008; Peng and Zou, 2011). In addition, large

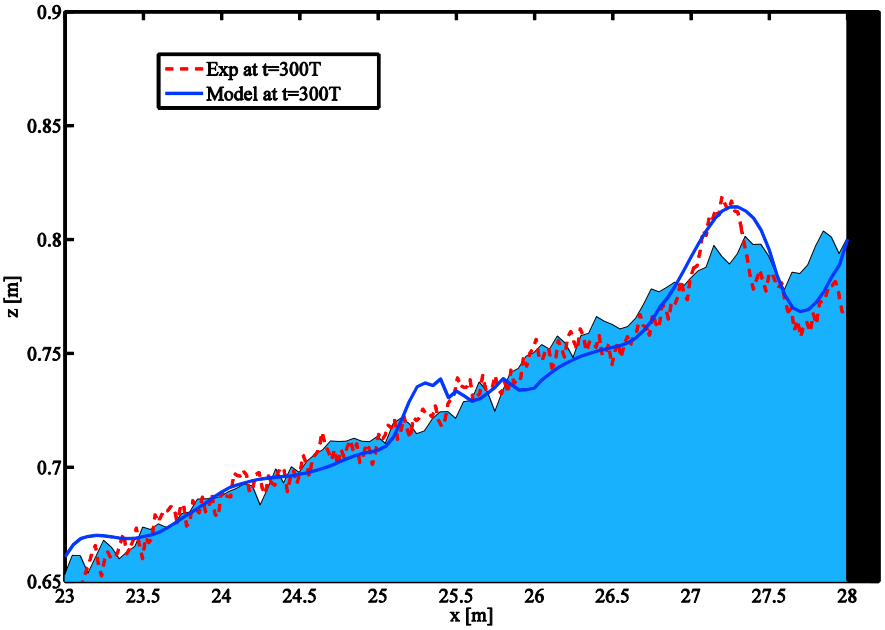

Fig. 20. Comparisons of the model results and measurements of bed profiles, with a significant wave height $H_s = 0.2\ m$, wave period $T_p = 1.87$ s, deep water depth $h_0 = 1.0\ m$ and water depth at the toe of the wall $h_{toe} = 0.2\ m$.

waves due to beach lowing would lead to larger wave loading which may cause structural failure by damaging the structural components of coastal defence and decrease the structural stability against overturning and sliding motions (Oumeraci, 1994, Peregrine 2003; Bullock et al., 2007; Bredmose et al 2010; Cuomo et al., 2010; Jiang et al., 2017). It is a worthwhile future work to carry out experiment and numerical study that focuses on the impact of beach lowering on wave loading and structure stability, and establish the relationship between these processes under various wave conditions.

6. Conclusions

In this study, a RANS-VOF model was coupled with a sediment transport and a morphological model to examine the hydrodynamics of wave interactions with a Seawall and the subsequent beach profile change and toe scour. A novel partial cell technique in analogy to the VOF method for free surface capturing scheme was applied to track the movement of water-soil interface. The partial cell approach has several advantages over the conventional method. For example, the model grids are fixed and the same set of orthogonal structured grids are used for morphological, sediment transport and hydrodynamic models. This approach avoids adapting grids to the evolving beach morphology and synchronizing different set of model grids as in previous studies, therefore, consumes less CPU. In addition, it improves model stability by minimizing the potential discontinuity problem at the evolving water–soil interface. The sand-slide model to resolve the sediment avalanche by Liang and Cheng (2005) is modified to improve the mass conservation of bed material. Moreover, the RANS-VOF model has been further extended to better cope with the complex bathymetry associated with beach morphological changes, such as a ripple bed.

The numerical results of a standing wave over a flat bottom compare well with theory. The well-known double circulating cells under the standing wave are reproduced by the present model. The predicted alternating streaming flow patterns is consistent with theory and previous studies. The present model is able to capture the observed alternating scour and deposition patterns in front of a Seawall on a flat bottom in the laboratory measurements. For waves propagating over a sloping beach in front of a Seawall, the model results of beach profile and toe scour are in good agreement with the measurements for a given wave condition and local water depth.

The good performance of the present model in this study proves the ability of the present model to simulate the toe scour in front of a vertical wall, on both flat bottom and sloping beaches. Unlike the depth-averaged phase resolving model, the present model is able to resolve wave breaking, turbulence, the vertical variation of flow, vortical motion of mean flow, and steady streaming, which play key roles in sediment transport.

More specifically, our model results led to the following key processes:

- The dominating physics of toe scour on a flat bottom is the double circulating cells due to standing waves, while the dominating physics of toe scour on a sloping beach are wave breaking, undertow, eddies in front of the wall and the partial standing wave; These physical processes are dependent on the incoming wave steepness, relative water depth at the toe of the vertical wall and beach slope.
- The model predicted toe scour on a flat bottom occurs between the first node and the vertical wall, while the model predicted deposition is at the first node;
- The plunging tongue of breaking wave is of key importance to toe scour. If the wave breaks near the wall, the plunging tongue would hit the wall and generate a jet downwards to deeply scour the toe of the wall. The location of wave breaking is thus a key parameter. Case 3 in section 4.2.3 has a breaking point around 2.5 m from the wall, while case 2 in section 4.2.2 has a breaking point around 1 m from the wall. It is evident from the model and experimental results that both the extent and maximum depth of the scour for case 2 are larger than those for case 3;
- If fewer waves break in the presence of relatively small waves and deep water, then the partial standing wave dominates the process, and the scour and deposition are mild as the near bed streaming velocity is rather small (e.g. case 1); if waves break near the toe of the vertical wall, then the near bottom streaming velocity away from the vertical wall with significant magnitude, leads to a significant scour and deposition pattern and toe scour (e.g. case 2); if waves break away from the vertical wall, then most of wave energy is dissipated before reaching the wall, and the partial standing wave dominates the process (e.g. case 3);
- The counter clock-wise eddies in front of the vertical wall moves the location of maximum scour depth away from the wall (case 1 and case 3), rather than direct at the toe of the wall (case 2). The incoming wave climbs and surges along the vertical wall. Once the surging wave jet turns around and falls into the water, it is carried away from the vertical wall by the near bottom undertow in the offshore direction. Therefore, the counter clock-wise eddies are formed.

As discussed in the previous section, the present model neglects the suspended sediment, therefore, the findings and conclusions may be valid only if the bedload instead of suspended sediment is the dominant contributing factor for the beach profile change and toe scour in front of the structure. However, the novel concept of partial cell technique is applicable even in the presence of suspended sediment as long as it is included in the sediment transport and bed level updating model.

This study sheds new light on the key processes governing beach morphological change and toe scour at a Seawall, and improves guidance on defence design to mitigate the scour around coastal structures. In the future, it is worth to examine the contribution of the suspended sediment transport to the toe scour in the presence of large breaking wave jets and fine sediments; explore the effect of beach slopes on toe scour in front of vertical walls by considering both uniform and non-uniform slopes, e.g. different slopes within swash zones and outside swash zones; and investigate the coupling of beach morphological change and toe scour with wave overtopping.

Acknowledgments

We are grateful to Drs J. Sutherland and C. Obhrai at HR Wallingford, who generously provided the laboratory measurements for the present work. This work benefits from discussions with Drs. A. Pedrozo-Acuna, D. Jones and Prof. D.E. Reeve. We are grateful for the support of the Physical Oceanography Program of National Science Foundation under Award Number 1436642 and the Maine Sea Grant and National Oceanic and Atmospheric Administration (Grants No. NA10OAR4170072) and the open fund of the State Key Laboratory of Hydraulics and Mountain River (Grant No. SKHL1311) at Sichuan University. The third author acknowledges the supported by NSFC (51279120).

Appendix

The Reynolds-Averaged Navier-Stokes (RANS) equations for an incompressible fluid are:

$$\frac{\partial \langle u_i \rangle}{\partial x_i} = 0 \tag{A.1}$$

$$\frac{\partial\langle u_i\rangle}{\partial t}+\langle u_j\rangle\frac{\partial\langle u_i\rangle}{\partial x_j}=-\frac{1}{\langle\rho\rangle}\frac{\partial\langle P\rangle}{\partial x_i}+\frac{1}{\langle\rho\rangle}\frac{\partial}{\partial x_j}\left(\mu\left(\frac{\partial\langle u_i\rangle}{\partial x_j}+\frac{\partial\langle u_j\rangle}{\partial x_i}\right)-\langle\rho\rangle\langle u_i'u_j'\rangle\right)+g_i \tag{A.2}$$

where '< >' represents the ensemble average, "′" represents the turbulent fluctuation, $<u_i>$ is the i-th component of the velocity vector (i, j = 1, 2 for a two dimensional problem), ρ is the fluid density, $<P>$ the mean pressure, g_i is the i-th component of the gravitational acceleration, μ the molecular dynamic viscosity, and $\langle u_i'u_j'\rangle$ is the Reynolds stress.

Reynolds stress closure model in this study is the so-called *k*-*ε* model in which Reynolds stress tensor is assumed to be related to the strain rate of the mean flow through the algebraic nonlinear Reynolds stress model (Shih et al., 1996). The *k*-*ε* model has been employed as it can provide the overall better simulation results for the wave shoaling and wave breaking simulation which the wave-induced bottom boundary layer can be reasonably captured, though k-omega model is more accurate within the turbulent boundary layer but its accuracy degenerates towards the free surface.

$$\frac{\partial k}{\partial t}+\langle u_j\rangle\frac{\partial k}{\partial x_j}=+\frac{\partial}{\partial x_j}\left[\left(\nu+\frac{\langle\nu_t\rangle}{\sigma_k}\right)\frac{\partial k}{\partial x_j}\right]-\langle u_i'u_j'\rangle\frac{\partial\langle u_i\rangle}{\partial x_j}-\varepsilon \tag{A.3}$$

$$\frac{\partial\varepsilon}{\partial t}+\langle u_j\rangle\frac{\partial\varepsilon}{\partial x_j}=C_{1\varepsilon}\frac{\varepsilon}{k}\nu_t\left(\frac{\partial\langle u_i\rangle}{\partial x_j}+\frac{\partial\langle u_j\rangle}{\partial x_i}\right)\frac{\partial\langle u_i\rangle}{\partial x_j}+\frac{\partial}{\partial x_j}\left[\left(\nu+\frac{\nu_t}{\sigma_\varepsilon}\right)\frac{\partial\varepsilon}{\partial x_j}\right]-C_{2\varepsilon}\frac{\varepsilon^2}{k} \tag{A.4}$$

where k is the turbulence kinetic energy and ε is the energy dissipation rate. The empirical coefficients that appear in the model are surprisingly universal. The recommended values for these coefficients are (Rodi, 1980): $C_d = 0.09$; $C_{1\varepsilon} = 1.44$; $C_{2\varepsilon} = 1.92$; $\sigma_k = 1.0$ and $\sigma_\varepsilon = 1.3$.

For the turbulence field, the exchange of turbulent kinetic energy and the turbulent dissipation rate at the free surface are assumed to be zero, that is,

$$\frac{\partial k}{\partial n}=0 \tag{A.5}$$

$$\frac{\partial\varepsilon}{\partial n}=0 \tag{A.6}$$

Near the solid boundary, the log-law distribution of mean tangential velocity in the turbulent boundary layer is applied, where the values of k and ε can be expressed as functions of the distance from the boundary and the mean tangential velocity outside of the viscous sub-layer:

$$\frac{\langle u\rangle}{u_*}=\frac{1}{\kappa}\ln\left(\frac{u_*y}{\nu}\right) \tag{A.7}$$

$$k=\frac{{u_*}^2}{\sqrt{C_d}} \tag{A.8}$$

$$\varepsilon=-\langle u'v'\rangle\frac{d\langle u\rangle}{dy}=\frac{{u_*}^3}{\kappa y} \tag{A.9}$$

$$\nu_t=-\frac{\langle u'v'\rangle}{\frac{\partial\langle u\rangle}{\partial y}}=\kappa u_* y \tag{A.10}$$

As mentioned by Lin and Liu (1998), the model will produce no turbulence energy if there is no turbulence kinetic energy initially. Both the initial condition and inflow boundary condition for k and ε are defined as: $k=\frac{1}{2}(\zeta c)^2$ and $\varepsilon=C_d k^2/(\xi\nu)$, where c is the wave celerity at the inflow boundary, ν is kinematic viscosity, $\zeta = 2.5\text{e-}3$, $\xi = 0.1$, $C_d = 0.09$. Lin and Liu (1998) found that the values of ζ and ξ have little impact on the numerical solutions away from the breaking point.

In the numerical simulation, the first grid point is normally located in the fully developed turbulent boundary layer with $y^+=\frac{u_*y}{\nu}>20$, in which the log-law is applied to relate the velocity to the shear velocity.

References

Sumer, B.M., Fredsøe, J., 2002. The Mechanics of Scour in the Marine Environment. Advanced Series on Ocean Engineering, vol. 17. World Scientific Publishing Co. Pte. Ltd.

Abbott, M.B., Basco, D.R., 1989. Computational Fluid Dynamics: an Introduction for Engineers. Longman Scientific & Technical, Harlow, Essex, England.

Bakhtyar, R., Ghaheri, A., Yeganeh-Bakhtiary, A., Barry, D.A., 2009. Process-based model for nearshore hydrodynamics, sediment transport and morphological evolution in the surf and swash zones. Appl. Ocean Res. 31 (1), 44–56.

Bakhtyar, R., Razmi, A.M., Barry, D.A., Yeganeh-Bakhtiary, A., Zou, Q.-P., 2010. Air-water two-phase flow modeling of turbulent surf and swash zone wave motions. Adv. Water Resour. 33 (12), 1560–1574. https://doi.org/10.1016/j.advwatres.2010.09.007.

Baldock, T., Alsina, J., Caceres, I., Vicinanza, D., Contestabile, P., Power, H., Sanchez-Arcilla, A., 2011. Large-scale experiments on beach profile evolution and surf and swash zone sediment transport induced by long waves, wave groups and random waves. Coast. Eng. 58 (2), 214–227.

Batchelor, G.K., 1967. An Introduction to Fluid Dynamics. Cambridge University Press.

Baykal, C., Sumer, B.M., Fuhrman, D.R., Jacobsen, N.G., Fredsøe, J., 2015. Numerical investigation of flow and scour around a vertical circular cylinder. Phil. Trans. R. Soc. A 373, 20140104. https://doi.org/10.1098/rsta.2014.0104.

Bredmose, H., Hunt-Raby, A., Jayaratne, R., Bullock, G.N., 2010. The ideal flip-through impact: experimental and numerical investigation. J. Eng. Math. 67, 115–136 special commemorative volume for Howell Peregrine.

Bullock, G.N., Obhrai, C., Peregrine, D.H., Bredmose, H., 2007. Violent breaking wave impacts. Part 1: results from large-scale regular wave tests on vertical and sloping walls. Coast. Eng. 54, 602–617.

Butt, T., Russell, P., 2000. Hydrodynamics and cross-shore sediment transport in the swash-zone of natural beaches: a review. J. Coast. Res. 16 (2), 255–268.

Christensen, E.D., 2006. Large eddy simulation of spilling and plunging breakers. Coast. Eng. 53 (5–6), 463–485.

CIRIA, 1986. Seawalls: Survey of Performance and Design Practice. Tech Note 125, ISBN 086017 266X, ISSN 0305 – 1718.

Craik, A.D.D., 1982. The drift velocity of water waves. J. Fluid Mech. 116, 187–205.

Cuomo, G., Allsop, W., Bruce, T., Pearson, J., 2010. Breaking wave loads at vertical sea walls and breakwaters. Coast. Eng. 57, 424–439.
Fredsøe, J., Deigaard, R., 1992. Mechanics of Coastal Sediment Transport. Advanced Series on *Ocean Engineering* 3. World Scientific.
Fredsøe, J., Sumer, B.M., 1997. Scour at the round head of a rubble-mound breakwater. Coast. Eng. 29 (3–4), 231–262.
Garcia, N., Lara, J.L., Losada, I.J., 2004. 2-D numerical analysis of near-field flow at low-crested permeable breakwaters. Coast. Eng. 51 (10), 991–1020.
Gislason, K., Fredsøe, J., Deigaard, R., Sumer, B.M., 2009a. Flow under standing waves: Part 1. Shear stress distribution, energy flux and standing waves. Coast. Eng. 56 (3), 341–362.
Gislason, K., Fredsøe, J., Sumer, B.M., 2009b. Flow under standing waves: Part 2. Scour and deposition in front of breakwaters. Coast. Eng. 56 (3), 363–370.
Gonzalez-Rodriguez, D., Madsen, O.S., 2007. Seabed shear stress and bedload transport due to asymmetric and skewed waves. Coast. Eng. 54, 914–929.
Hajivalie, F., Yeganeh-Bakhtiary, A., 2009. Numerical study of breakwater steepness effect on the hydrodynamics of standing waves and steady streaming. J. Coast. Res. SI 56, 514–518.
Hajivalie, F., Yeganeh Bakhtiary, A., Houshanghi, H., Gotoh, H., 2012. Euler-lagrange model for scour in front of vertical breakwater. Appl. Ocean Res. 34, 96–106.
Hsu, T.J., Liu, P.L.F., 2004. Toward modeling turbulent suspension of sand in the nearshore. J. Geophys. Res.-Oceans 109 (C6), CO6018.
Jacobsen, N.G., 2015. Mass conservation in computational morphodynamics: uniform sediment and infinite availability. Int. J. Numer. Meth. Fluids 78, 233–256. https://doi.org/10.1002/fld.4015.
Jacobsen, N.G., Fuhrman, D.R., Fredsøe, J., 2012. A wave generation toolbox for the open-source CFD library: OpenFoam®. Int. J. Numer. Meth. Fluids 70, 1073–1088. https://doi.org/10.1002/fld.2726.Jacobsen.
Jacobsen, N.G., Fredsøe, J., Jensen, J.H., 2014a. Formation and development of a breaker bar under regular waves. Part 1: model description and hydrodynamics. Coast. Eng. 88, 182–193.
Jacobsen, N.G., Fredsøe, J., Jensen, J.H., 2014b. Formation and development of a breaker bar under regular waves. Part 2: model description and hydrodynamics. Coast. Eng. 88, 55–68.
Jasak, H., 1996. Error Analysis and Estimation for the Finite Volume Method with Applications to Fluid Flows. Ph.D. thesis. Imperial College London, p. 394.
Jiang, X.L., Zou, Q.P., Zhang, N., 2017. Wave load on submerged quarter-circular and semicircular breakwaters under irregular waves. Coast. Eng. 121, 265–277. https://doi.org/10.1016/j.coastaleng.2016.11.006. ISSN 0378-3839.
Khosronejad, A., Kang, S., Sotiropoulos, F., 2012. Experimental and computational investigation of local scour around bridge piers. Adv. Water Resour. 37, 73–85.
Lara, J.L., Garcia, N., Losada, I.J., 2006. RANS modelling applied to random wave interaction with submerged permeable structures. Coast. Eng. 53 (5–6), 395–417.
Larson, M., Kubota, S., Erikson, L., 2001. A model of sediment transport and profile evolution in the swash zone. In: Hanson, H., Larson, M. (Eds.), Coastal Dynamics '01. ASCE, Lund, Sweden, pp. 908–917.
Liang, D., Cheng, L., 2005. Numerical model for wave-induced scour below a submarine pipeline. J. Waterw. Port, Coast. Ocean Eng. 131 (5), 193–202.
Lin, P.Z., Liu, P.L.F., 1998. A numerical study of breaking waves in the surf zone. J. Fluid Mech. 359, 239–264.
Lin, P.Z., Liu, P.L.F., 2003. Discussion of "Vertical variation of the flow across the surf zone". Coast. Eng. 50 (3), 161–164. January 2004.
Liu, X., García, M.H., 2008. A 3D numerical model with free water surface and mesh deformation for local sediment scour. J. Waterw. Port, Coast. Ocean Eng. 134 (4), 203–217.
Long, W., Kirby, J.T., Shao, Z., 2008. A numerical scheme for morphological bed level calculations. Coast. Eng. 55 (2), 167–180.
Longuet-Higgins, M.S., 1953. Mass transport in water waves. Philos. Trans. Roy. Soc. Lond. A245, 535–581.
Losada, I.J., Lara, J.L., Guanche, R., Gonzalez-Ondina, J.M., 2008. Numerical analysis of wave overtopping of rubble mound breakwaters. Coast. Eng. 55 (1), 47–62.
Lubin, P., Vincent, S., Abadie, S., Caltagirone, J.P., 2006. Three-dimensional large eddy simulation of air entrainment under plunging breaking waves. Coast. Eng. 53, 631–635.
Madsen, O.S., 1991. Mechanics of cohesionless sediment transport in coastal waters. In: Kraus, N.C. (Ed.), Proceedings of Coastal Sediments 91'. ASCE, Seattle, Washington, pp. 15–27.
Madsen, O.S., 1994. Spectral wave-current bottom boundary layer flows. In: Proc. ASCE 24th Int. Conf. On Coastal Engineering (ICCE), Kobe, Japan. ASCE, pp. 384–398.
Marieu, V., Bonneton, P., Foster, D.L., Ardhuin, F., 2008. Modeling of vortex ripple morphodynamics. J. Geophys. Res. 113, C09007 https://doi.org/10.1029/2007JC004659.
Meyer-Peter, E., Mueller, R., 1948. Formulas for bed load transport. In: Second Meeting of the International Association of Hydraulic Structures, Stockholm, Sweden, pp. 39–64.
Oumeraci, H., 1994. Review and analysis of vertical breakwater failures – lessons learned. Coast. Eng. 22, 3–29.
Pedrozo-Acuña, A., Simmonds, D.J., Otta, A.K., Chadwick, A.J., 2006. On the cross-shore profile change of gravel beaches. Coast. Eng. 53 (4), 335–347.
Pedrozo-Acuna, A., Torres-Freyermuth, A., Zou, Q.-P., Hsu, T.-J., Reeve, D.E., 2010. Diagnostic investigation of impulsive pressures induced by plunging breakers impinging on gravel beaches. Coast. Eng. 57 (3), 252–266. https://doi.org/10.1016/j.coastaleng.2009.09.010.
Peng, Z., 2010. Transformation of Wave Shape and Spatial Distribution of Wave Overtopping Water over a Coastal Structure. PhD thesis. University of Plymouth.
Peng, Z., Zou, Q.-P., 2011. Spatial distribution of wave overtopping water behind coastal structures. Coast. Eng. 58 (6), 489–498.
Peregrine, D.H., 2003. Water-wave impact on walls. Annu. Rev. Fluid Mech. 35, 23–43.
Pullen, T., Allsop, W., Bruce, T., Pearson, J., 2008. Field and laboratory measurements of mean overtopping discharges and spatial distributions at vertical seawalls. Coast. Eng. 56 (2), 121–140.
Rakha, K.A., Kamphuis, J.W., 1997. A morphology model for an eroding beach backed by a seawall. Coast. Eng. 30 (No. 1–2), 53–75.
Riley, N., 2001. Steady streaming. Annu. Rev. Fluid Mech. 33, 43–65.
Rodi, W., 1980. Turbulence Models and Their Application in Hydraulics – a State-of-the-art Review. IAHR Publication.
Roelvink, J.A., Reniers, A., van Dongeren, A., van Thiel De Vries, J., Lescinski, J., McCall, R., 2010. XBeach Model Description and Manual. Delft, The Netherlands.
Scott, C.P., Cox, D.T., Maddux, T.B., Long, J.W., 2005. Large-scale laboratory observations of turbulence on a fixed barred beach. Meas. Sci. Technol. 16 (10), 1903–1912.
Shih, T.H., Zhu, J., Lumley, J., 1995. A new Reynolds stress algebraic equation model. Comp. Meth. Appl. Mech. Eng. 125 (1), 287–302.
Smyth, C., Hay, A.E., 2003. Near-bed turbulence and bottom friction during SandyDuck97. J. Geophys. Res. 108 (C6), 3197. https://doi.org/10.1029/2001JC000952.
Soulsby, R.L., 1997. Dynamics of Marine Sands. Thomas Telford, London. ISBN 07277 2584 X.
Sumer, B.M., 2007. Mathematical modelling of scour: a review. J. Hydraul. Res. 45 (6), 723–735.
Sumer, B.M., Fredsøe, J., 2000. Experimental study of 2D scour and its protection at a rubble-mound breakwater. Coast. Eng. 40, 59–87.
Sutherland, J., Obhrai, C., Whitehouse, R.J.S., Pearce, A.M.C., 2006. Laboratory tests of scour at a seawall. In: Proceedings, 3rd International Conference on Scour and Erosion.
Tofany, N., Ahmad, M.F., Mamat, M., 2014. Simulation of scouring in front of an impermeable vertical breakwater using the RANS-VOF numerical model. J. Environ. Sci. Technol. 7 (6), 314–325.
Tofany, N., Ahmad, M.F., Mamat, M., Mohd-Lokman, H., 2016. The effects of wave activity on overtopping and scouring on a vertical breakwater. Ocean. Eng. 116, 295–311.
Torres-Freyermuth, A., Lara, J.L., Losada, I.J., 2010. Numerical modelling of short- and long-wave transformation on a barred beach. Coast. Eng. 57 (3), 317–330.
Troch, P., De Rouck, J., 1999. An active wave generating-absorbing boundary condition for VOF type numerical model. Coast. Eng. 38 (4), 223–247.
Tsai, C.-P., Chen, H.-B., You, S.-S., 2009. Toe scour of seawall on a steep seabed by breaking waves. J. Waterw. Port, Coast. Ocean Eng. 135 (2), 61–68.
Ünlüata, Ü., Mei, C.C., 1970. Mass transport in water waves. J. Geophys. Res. 75, 7611–7618.
Wang, Z.Y., Zou, Q.-P., Reeve, D.E., 2009. Simulation of spilling breaking waves using a two phase flow CFD model. Comput. Fluids 38 (10), 1995–2005.
Watanabe, A., Shiba, K., Isobe, M., 1994. A numerical model of beach change due to sheet-flow. In: Proc. 24th Int. Conf. On Coastal Eng. ASCE, pp. 2785–2798.
Weller, H.G., Tabor, G., Jasak, H., Fureby, C., 1998. A tensorial approach to computational continuum mechanics using object-oriented techniques. Comput. Phys. 12 (6), 620–631. https://doi.org/10.1063/1.168744.
Xie, Z., 2012. Numerical study of breaking waves by a two-phase flow model. Int. J. Numer. Methods Fluids 70, 246–268.
Yeganeh-Bakhtiary, A., Hajivalie, F., Hashemi-Javan, A., 2010. Steady streaming and flow turbulence in front of vertical breakwater with wave overtopping. Appl. Ocean Res. 32 (1), 91–102.
Young, D.M., Testik, F.Y., 2009. Onshore scour characteristics around submerged vertical and semicircular breakwaters. Coast. Eng. 56 (no. 8), 868–875. https://doi.org/10.1016/j.coastaleng.2009.04.003.
Youngs, D.L., 1982. Time-dependent multi-material flow with large fluid distortion. In: Morton, K.W., Baines, M.J. (Eds.), Numerical Methods for Fluid Dynamics. Academic Press, London, pp. 273–285.
Zhao, Q., Armfield, S., Tanimoto, K., 2004. Numerical simulation of breaking waves by a multi-scale turbulence model. Coast. Eng. 51 (1), 53–80.
Zou, Q.-P., 2002. An analytical model of wave bottom boundary layers incorporating turbulent relaxation and diffusion effects. J. Phys. Oceanogr. 32 (No. 9), 2441–2456. https://doi.org/10.1175/1520-0485(2002)032.
Zou, Q.-P., 2004. A simple model for random wave bottom friction and dissipation. J. Phys. Oceanogr. 34 (No. 6), 1459–1467. https://doi.org/10.1175/1520-0485(2004)034.
Zou, Q.-P., Peng, Z., 2011. Evolution of wave shape over a low-crested structure. Coast. Eng. 58 (6), 478–488. https://doi.org/10.1016/j.coastaleng. 2011.01.00.
Zou, Q.-P., Reeve, D.E., 2009. Modelling water from clouds to coast. Planet Earth, Nat. Environ. Res. Council (August issue), 22–23.
Zou, Q.-P., Peng, Z., Lin, P., 2012. Effects of wave breaking and beach slope on toe scour in front of a vertical seawall. In: The Proceedings of the 33rd International Conference on Coastal Engineering, Santander, Spain.
Zou, Q.-P., Chen, Y., Cluckie, I., Hewston, R., Pan, S., Peng, Z., Reeve, D., 2013. Ensemble prediction of coastal flood risk arising from overtopping and scour by linking meteorological, ocean, coastal and surf zone models. Q. J. R. Meteorol. Soc. 139 (671), 298–313. https://doi.org/10.1002/qj.2078.